PERGAMON

Available online at www.sciencedirect.com
SCIENCE DIRECT

Deep-Sea Research I 50 (2003) 371–395

DEEP-SEA RESEARCH
PART I

www.elsevier.com/locate/dsr

Observation of wave-enhanced turbulence in the near-surface layer of the ocean during TOGA COARE

Alexander Soloviev[a,*], Roger Lukas[b]

[a] *Oceanographic Center, Nova Southeastern University, 8000 North Ocean Drive, Dania Beach, FL 33004, USA*
[b] *Department of Oceanography, University of Hawaii, 1000 Pope Road, Honolulu, HI 96822, USA*

Received 14 June 2002; received in revised form 20 December 2002; accepted 20 December 2002

Abstract

Dissipation rate statistics in the near-surface layer of the ocean were obtained during the month-long COARE Enhanced Monitoring cruise with a microstructure sensor system mounted on the bow of the research vessel. The vibration contamination was cancelled with the Wiener filter. The experimental technique provides an effective separation between surface waves and turbulence, using the difference in spatial scales of the energy-containing surface waves and small-scale turbulence. The data are interpreted in the coordinate system fixed to the ocean surface. Under moderate and high wind-speed conditions, we observed the average dissipation rate of the turbulent kinetic energy in the upper few meters of the ocean to be 3–20 times larger than the logarithmic layer prediction. The Craig and Banner (J. Phys. Oceanogr. 24 (1994) 2546) model of wave-enhanced turbulence with the surface roughness length from the water side z_0 parameterized according to the Terray et al. (J. Phys. Oceanogr. 26 (1996) 792) formula $z_0 = cH_s$ provides a reasonable fit to the experimental dissipation profile, where z is the depth (defined here as the distance to the ocean surface), $c \approx 0.6$, and H_s is the significant wave height. In the wave-stirred layer, however, the average dissipation profile deviates from the model (supposedly because of extensive removing of the bubble-disturbed areas close to the ocean surface). Though the scatter of individual experimental dissipation rates (10-min averages) is significant, their statistics are consistent with the Kolmogorov's concept of intermittent turbulence and with previous studies of turbulence in the upper ocean mixed layer.

Keywords: Turbulence; Wave breaking; Surface roughness; Dissipation rate

1. Introduction

Breaking surface waves generate strong turbulence in the near-surface layer of the ocean. In addition, these same waves create serious disturbances to turbulence measurements. Bubble clouds and random, sometimes huge, vertical motions of the ocean surface due to surface waves seriously complicate collection of quality turbulence data close to the ocean surface.

The velocity scale of turbulent fluctuations in the near-surface layer of the ocean is about $1\,\mathrm{cm\,s^{-1}}$, while the typical surface-wave orbital velocities are $1\,\mathrm{m\,s^{-1}}$. The energy of the disturbance due to surface-wave orbital velocities is four orders of magnitude higher than that of the

*Corresponding author. Tel.: +1-954-262-3659; fax: +1-954-262-4098.
E-mail address: soloviev@ocean.nova.edu (A. Soloviev).

0967-0637/03/$ - see front matter
doi:10.1016/S0967-0637(03)00004-9

turbulence signal. In terms of the dissipation rate of turbulent kinetic energy (TKE), ε, the surface-wave disturbance is six orders of magnitude greater than the useful signal. The presence of such exceptionally strong disturbances from the surface-wave orbital velocities imposes special requirements on the measurement techniques and sensors for observations of near-surface turbulence. The additional complication is that the time scales of the surface waves and the near-surface boundary-layer turbulence substantially overlap. The linear statistical filtering that has been widely used to separate waves and turbulence from moored or tower-based velocity records (e.g., Benilov and Filyushkin, 1970; Kitaigorodskii et al., 1983) is capable of distinguishing the turbulence from linear waves. This linear filtering procedure, however, cannot remove non-linear components of surface waves, which may result in an overestimation of the turbulence dissipation rate.

Stewart and Grant (1962) demonstrated that towed or bow measurements can provide an effective separation between the surface waves and turbulence. Their techniques utilize the fact that the energy-containing surface waves and small-scale turbulence in the near-surface layer of the ocean have different spatial scales.

The Stewart and Grant (1962) results indicated that the wave-generated turbulence essentially dissipates above the trough line. A similar conclusion was reached by Soloviev et al. (1988) based on the dimensional analysis of dissipation rate profiles obtained with a free-rising profiler and of the observations made by Arsenyev et al. (1975), Dillon et al. (1981), Oakey and Elliott (1982), and Jones and Kenney (1977). These analyzed data, however, were confined to moderate and low wind-speed conditions. At the same time, tower-based turbulence measurements made in a lake by Kitaigorodskii et al. (1983) and Agrawal et al. (1992) in a wide range of wind-speed conditions produced evidence in favor of a thicker layer of wave-enhanced turbulence and higher turbulence levels. Terray et al. (1996) proposed the new scaling that accounted for the limited fetch in the lake observations and dramatically reduced the difference between the two groups of data.

Though new turbulence data in the near-surface layer of the open ocean are emerging (Drennan et al., 1996; Greenan et al., 2001; Gemmrich and Farmer, 2002; Melville and Matusov, 2002), most of the published turbulence statistics have been obtained either in lakes and shallow seas or under relatively low wind-speed conditions. In this paper, we present the month-long near-surface turbulence data set taken in the western equatorial Pacific during the TOGA Coupled Ocean–atmosphere Response Experiment (COARE) under a variety of forcing and mixed layer conditions. The subset of this data that was obtained under high wind-speed conditions allows us to estimate and parameterize the turbulence levels due to surface-wave breaking. Although our observations have been made in the tropical and equatorial ocean, the conclusions of this paper are expected to be applicable to the mid- and high-latitudes as well.

2. Observations during the COARE EQ-3 cruise

The TOGA COARE was conducted in the western equatorial Pacific warm pool area during 1992–1994. The large scale context for the TOGA COARE is summarized by Lukas et al. (1995), and a comprehensive overview of the results is provided by Godfrey et al. (1998).

A near-surface microstructure sensor system (Soloviev et al., 1995, 1998, 1999) was mounted on the bow of the R/V. *Moana Wave* during the COARE enhanced monitoring cruise EQ-3, which consisted of two legs (Fig. 1). The EQ-3 cruise is briefly described below; more cruise details can be found in Shinoda et al. (1995).

On 11 April 1994, the R/V. *Moana Wave* departed Pohnpei for Leg 1. Leg 1 included mooring operations and CTD stations between 8°N and 2°S (Fig. 1). Leg 1 ended on 25 April in Pohnpei. Leg 2 of the EQ-3 cruise started in Pohnpei on 26 April 1994. Leg 2 included a southward transect along 156°E, an equatorial transect from 154°E to 143°E, and a short northward transect along 137°E before arrival in Guam on 10 May 1994. Underway operations during both legs included the microstructure

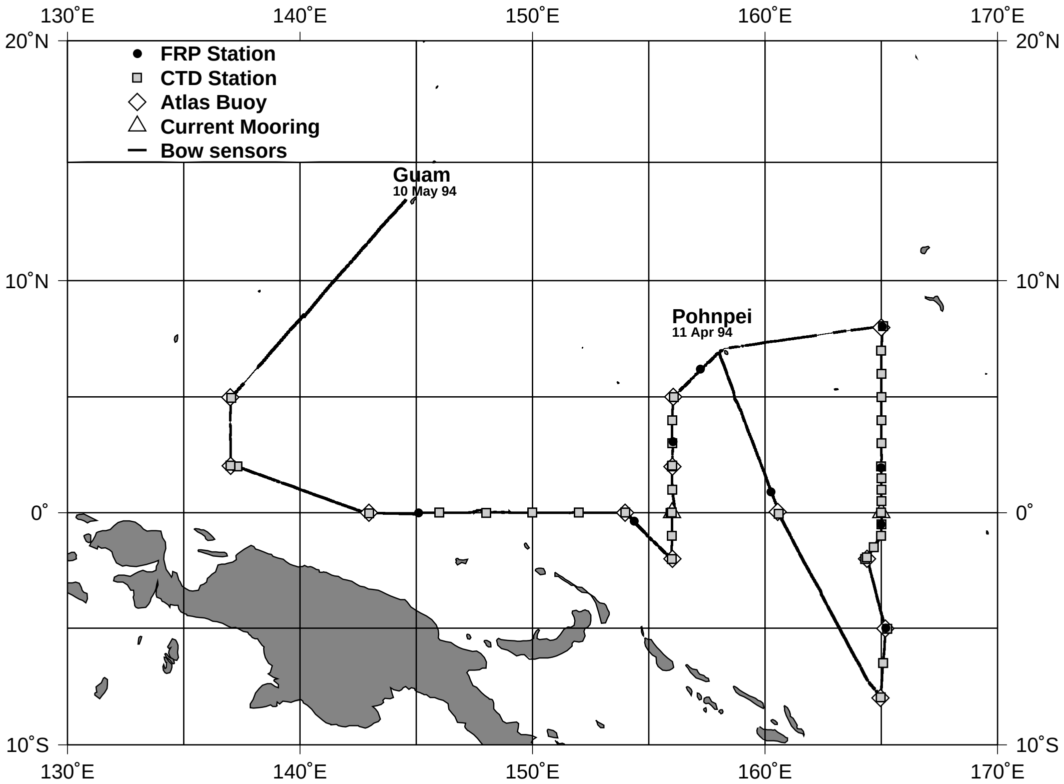

Fig. 1. Map of the COARE enhanced monitoring EQ-3 cruise of the R/V. *Moana Wave*.

and turbulence bow sensor measurements, thermosalinograph sampling, shipboard ADCP and meteorological observations. Many aspects of the near-surface microstructure measurements during the EQ-3 cruise have been analyzed by Soloviev and Lukas (1996, 1997a, b). These analyses have elucidated large diurnal warming events in the near-surface layer of the ocean, spatial variability of the diurnal thermocline, and sharp frontal interfaces. In this paper, we analyze the near-surface turbulence measurements taken during the EQ-3 cruise with the bow sensors.

For the analysis of near-surface turbulence dissipation rates, the significant wave height and friction velocity are important parameters. The significant wave height H_s is estimated from the pressure and vertical acceleration bow sensor signals as described in Appendix A. Fig. 2a documents the significant wave height data for the time period of the *Moana Wave* EQ-3 cruise in comparison with the occasional TOPEX/Poseidon data. The technique for estimation of the significant wave height from the TOPEX/Poseidon satellite observations has been validated by Callahan et al. (1994).

Because of the unresolved short-wave part of the surface-wave spectrum, the relative error of the H_s estimation from the bow data dramatically increases under low wind-speed conditions (Fig. 13). For the further analysis involving H_s as a parameter we will use a 20% error threshold, which, according to Appendix A (Fig. 13), corresponds to a 9.4 m s^{-1} wind speed.

Four meteorological data sets are available for the EQ-3 cruise (Fig. 2b). An automatic meteorological station provided 5-min averages of wind speed at a 15 m height (further referred to as U_{15}). The meteorological data were also collected by the science group at 6-h intervals and from bridge observers at 4-h intervals. Occasional wind-speed

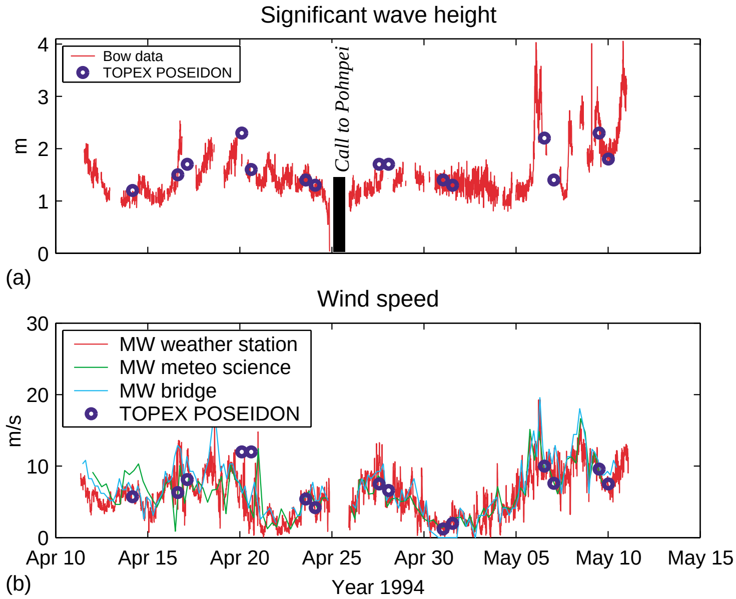

Fig. 2. R/V. *Moana Wave* and TOPEX POSEIDON (a) significant wave height and (b) wind-speed data for COARE EQ-3. The crossover distance between the satellite and research vessel trajectories varies between 22 and 440 km. The interruption of measurements between 25 and 26 April is because of a 1 day call of the research vessel to the Port of Pohnpei. Note the drop of significant wave height to zero at the entrance to the Port.

magnitudes were available from the TOPEX/Poseidon satellite.

A 10° offset in the wind sensor data was discovered on 23 April 1994 (10° lower than it should be). This offset might result in about $1\,\mathrm{m\,s^{-1}}$ error in the wind-speed measurement at the typical 12-knot ship speed. In this paper, we analyze the turbulence measurements taken under high wind-speed conditions and have not made any correction of this possible offset.

The friction velocity was calculated from the COARE bulk-flux 2.6 algorithm (Fairall et al., 2003). We interpolated the drag coefficient during the EQ-3 cruise with a fourth-order polynomial as follows:

$$C_a = -7.1510\times10^{-9}U_{15}^4 + 2.4086\times10^{-7}U_{15}^3 - 9.1358\times10^{-7}U_{15}^2 + 2.39\times10^{-5}U_{15} + 9.320\times10^{-4}.$$

For high wind-speed conditions, the difference between C_a calculated from the COARE 2.6 algorithm and its polynomial interpolation does not exceed 2%.

3. Turbulence measurements using bow-mounted sensors

3.1. Experimental approach

The orbital velocities of surface waves are the dominant disturbance to turbulence measurements in the near-surface layer of the ocean. They influence turbulence measurements by (a) generating an additive fluctuation velocity signal, and (b) modulating the relative speed (and direction) of the flow.

In the case of tower-based and mooring measurements, the velocity fluctuation induced by the orbital velocities of surface waves usually exceeds the mean drift current. Taylor's (1938) frozen field approximation, which requires that the fluctuation of the mean flow is within 10% of its mean speed, cannot be satisfied for this type of measurement; the standard techniques of turbulence analysis, therefore, are not applicable. Moreover, in the case of tower-based or mooring measurements, the time scales of turbulence and surface-wave signals substantially overlap. Problem (a), nevertheless, can be solved by a linear statistical analysis (Benilov and Filyushkin, 1970; Agrawal et al., 1992); problem (b), which requires a non-linear statistical analysis, is much more difficult and has not yet been solved for the tower or mooring based observations.

It is remarkable that spatial scales of turbulence and surface waves may differ greatly. As a result, both problems (a) and (b), can be resolved by making turbulence measurements with a fast-moving sensor (Stewart and Grant, 1962; Soloviev et al., 1988). The experimental approach adopted in this work is as follows (Soloviev et al., 1999):

(1) turbulence measurements are acquired with a fast-moving sensor;
(2) sensors with linear output are used; and
(3) the coordinate system is fixed to the ocean surface.

A specially constructed bow frame positioned the sensor system at a 2-m distance ahead of the ship's hull (Fig. 3). The pressure wave in front of the moving ship may result in a *rapid flow distortion* (Fornwalt et al., 2002). The bow of the R/V. *Moana Wave* is of a sharp-angle (30°) shape, the curvature radius of the bow tip is about 0.2 m. From classical hydrodynamics it is known that the flow in front of a moving sphere is significantly disturbed within approximately 3 radii of the sphere (Van Dyke, 1982). This suggests that the bow sensor data were taken from the area that is not significantly disturbed by ship's hydrodynamics.

The sensor package consisted of an electromagnetic (EM) velocity probe (including an accelerometer and a CTD). The EM velocity sensor, originally developed in *Granit* (St. Petersburg, Russia) by Arjannikov et al. (1979), has a perfect hydrodynamic form for longitudinal direction and a low hydrodynamic noise level. This probe is a linear device for a wide flow-speed range (0–12.5 m s^{-1}); the spatial resolution is about 1 cm.

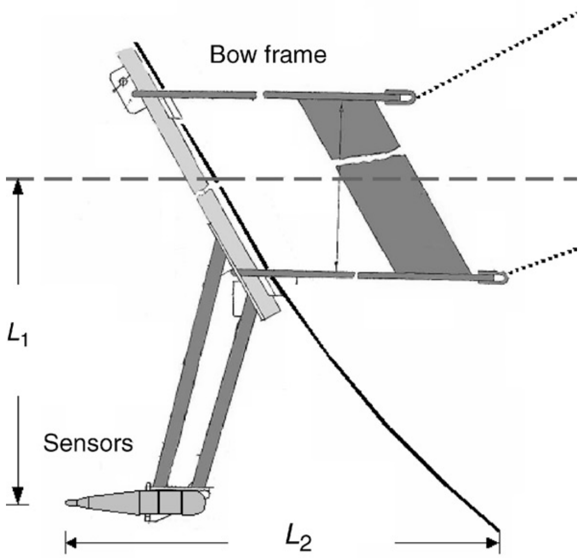

Fig. 3. Schematic diagram showing the probe mounting on the bow. Mean depth of the probe $L_1 \approx 1.7$ m, spacing from the ship's hull $L_2 \approx 2$ m.

According to the laboratory test conducted at the University of Hawaii, the electronic noise level of the EM velocity sensor in the frequency range 2–400 Hz is equivalent to 0.8 mm s^{-1}. More details about the EM probe and the CTD can be found in Soloviev et al. (1998, 1999).

Ship's pitching and surface waves (including those reflected from the ship's hull) induce fluctuations of the mean flow at the sensor location. A strong fluctuation may result in flow reversal, which affects the turbulence measurements. To identify such cases, we analyzed a sum $U_0 + V_x$ (where U_0 is the ship speed and V_x is the longitudinal component of the bow velocity signal). Negative values of $U_0 + V_x$ are the flow reversals; these record segments were removed from further analysis. The flow reversals were found mainly at low ship speeds. We therefore did not analyze any data taken at $U_0 < 2$ m s^{-1}. (In fact, most of the data being analyzed in this paper were taken at $U_0 \sim 5$ m s^{-1}.)

The mean depth of the sensors was about 1.7 m but slightly varied during the cruise, depending on the filling of the ship's fuel and water tanks and ship speed. Because of surface waves and ship's pitching, the instantaneous depth of the sensors (defined here as the distance to the ocean surface) was continuously changing. The pressure signal was used to estimate the distance of the sensor to the ocean surface. Special precautions were made to reduce the direct influence of the water flow on the pressure sensor. An rms uncertainty of <0.1 dbar in pressure to depth conversion at a ship speed of 10–11 knots was estimated from the pressure readings at the intersections of the water–air interface as detected by the conductivity sensor (Soloviev and Lukas, 1996). The sensor depth variation allows us to study the vertical structure of the near-surface layer of the ocean.

3.2. Signal processing

The data analyzed in this paper were collected at a sampling rate of 400 or 40 Hz. Because of pitching of the vessel, at times the sensors broke through the surface. The segments of signal corresponding to the probe surfacing or entering bubble clouds were removed from the analysis according to the algorithm described in Soloviev et al. (1995). A significant part of the TKE in the near-surface layer dissipates within the actively breaking waves that produce bubble clouds. Removing the segments affected by bubbles may therefore introduce a bias in the turbulence statistics. This problem will be considered in Section 4.

Fig. 4a demonstrates an example of the V_x-velocity spectra calculated from a 10-min segment obtained at $5.5\,\mathrm{m\,s^{-1}}$ ship speed and at $4\,\mathrm{m\,s^{-1}}$ wind speed. For spectral calculations, the measured velocity data set was "pre-whitened" by numerical differentiation in the time domain and then integrated in the frequency domain. The pre-whitening is a procedure aimed at reducing spectral "leakage" (Emery and Thompson, 1998).

For comparison, the spectrum of integrated acceleration is shown in Fig. 4a. The acceleration spectrum suggests that the vibration contamination occurs in narrow frequency bands. Further evidence of the nature and degree of the vibration contamination can be seen in the plot of the coherence between the velocity and integrated acceleration, as shown in Fig. 4c. The velocity contamination at frequencies less than 1 Hz is associated with the ship's motion and is out of the band used for turbulence estimates. Above 8 Hz, there is a varying degree of contamination, with high coherence at 18, 25, 50 and 110 Hz. Removal of this vibration contamination by extrapolation of the spectrum through known motion peaks or with a notch filter turns out to be relatively ineffective here because the resonant properties of the bow frame depend on the position of the air–water interface with respect to the frame, which changes during the pitching period. Instead, we used the coherent noise cancellation technique, based on the Wiener filter, developed by Schoeberlein and Baker (1996) and tested with the TOGA COARE bow data in Soloviev et al. (1999). A similar noise cancellation technique for oceanic turbulence measurements has been developed by Rolf Lueck (pers. comm.).

One important aspect of implementing the Wiener filter is to insure that the reference correlation matrix is not singular and thus can be inverted. This can be a problem when data that contain a strong low-frequency component, such as the ship's motion and the surface-wave velocities at frequencies less than 1 Hz, are used. To avoid this problem, the data were pre-whitened by numerical differentiation. To restore the velocity spectrum after the coherent noise cancellation, the signal was integrated (either in the time or frequency domain).

Fig. 4b shows the velocity spectrum after application of the coherent noise cancellation techniques using the Wiener filter with 60 weights; Fig. 4d presents the residual coherence. Note that the 95% confidence intervals of the coherence enclose zero. This means that no statistically significant coherent contamination is left in the filtered signal. The effectiveness of the Wiener filter in the time domain is demonstrated in Fig. 5.

In Fig. 6a, the spectrum of the velocity signal processed with the Wiener filter as described above is compared to the electronics noise spectrum of the sensor. The corresponding 95% confidence intervals are shown with thin lines. The confidence intervals for the spectral estimates calculated from 10-min velocity segments are very small because the number of degrees of freedom is large (234).

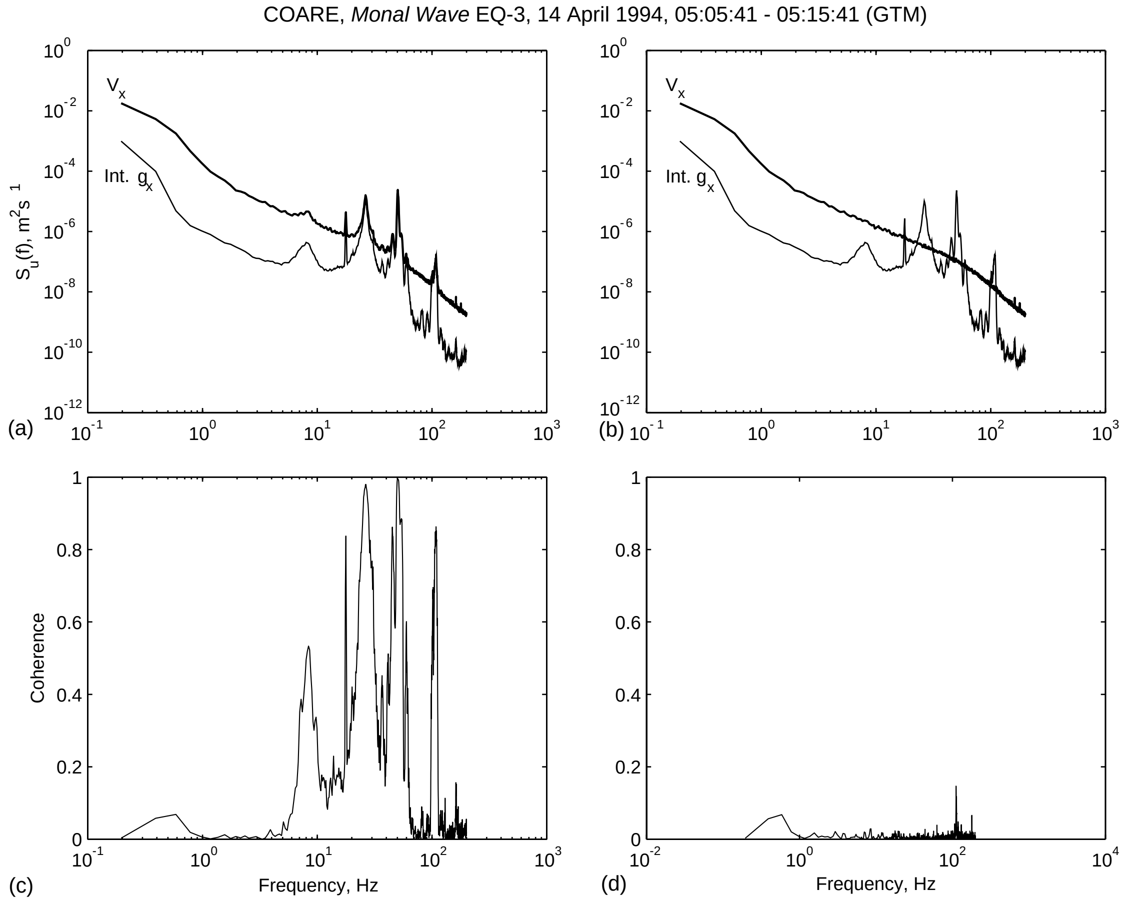

Fig. 4. Spectra of longitudinal velocity and integrated acceleration (a) before and (b) after the coherence noise reduction using the Wiener filter. The coherence function between these two signals (c) before and (d) after filtering reveals practically complete cancellation of the ship vibrations in the velocity signal.

The noise spectrum shown in Fig. 6a was measured in a laboratory tank with motionless sea water during the post-cruise calibration made with the same experimental setup. According to this laboratory test, the RMS noise for the V_x channel in the frequency range 2–200 Hz is $0.8\,\mathrm{mm\,s^{-1}}$.

Since the electronic noise and the measured velocity signal are not correlated, the noise spectrum can be subtracted from the V_x velocity spectrum. However, if the experimental spectrum is close to its noise level, this procedure may result in unrealistic negative spectral components at some frequencies. We will subtract the noise spectrum from the velocity spectrum here only for demonstration purposes. The spectrum is then corrected for the anti-aliasing filter. The transfer function of the anti-aliasing filter is $H_{\mathrm{lp}}(f) = 1/[1 + (f/f_{\mathrm{up}})^2]$, where $f_{\mathrm{up}} = 150\,\mathrm{Hz}$ for $f_s = 400\,\mathrm{Hz}$, $f_{\mathrm{up}} = 14.5\,\mathrm{Hz}$ for $f_s = 40\,\mathrm{Hz}$, and f_s is the sampling rate. The correction factor $H_{\mathrm{lp}}(f)^{-1}$ is shown in Fig. 6b for both 400-Hz (curve 1) and 40-Hz (curve 1′) sampling rates.

The frequency spectrum was transformed into the wave-number domain according to Taylor's (1938) frozen field hypothesis:

$$k_x = 2\pi f U_0^{-1}, \quad E(k_x) = (2\pi)^{-1} S(f) U_0, \tag{1}$$

where f is the frequency in Hz, U_0 is the relative flow speed (towed or mean flow advection speed), and k_x is the wave number in m^{-1}. Everywhere in

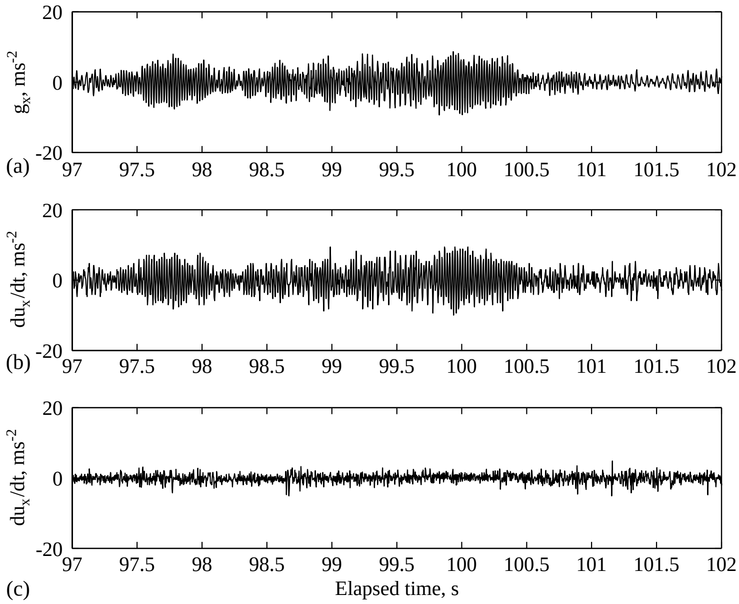

Fig. 5. Illustration of the coherent noise cancellation techniques in the time domain. This is a 5-s segment from the 10-min record used for spectral calculations in the example shown in Fig. 4. (a) Acceleration, (b) original velocity derivative signals, and (c) velocity derivative signal after the coherent noise cancellation using the Wiener filter. The acceleration signal is shown on the same scale as that of the velocity derivative.

this paper we use the radian wave number, $k = 2\pi/\lambda$. Taylor's hypothesis is acceptable if the RMS variation of the flow does not exceed 10% of the mean flow speed.

The wave-number spectrum was corrected for the sensor's spatial averaging according to the transfer function, $T(k_x) = (1 + (k_x/k_0)^{1.5})^{-2.8}$, $k_0 = 250\,\mathrm{m}^{-1}$, determined from laboratory tests (Soloviev et al., 1999). The resulting correction factor $T(k_x)^{-1}$ is shown in Fig. 6b as curve 2; thin lines indicate the error interval. Fig. 6b contains both frequency and wave-number scales. The wave-number axes are calculated for $U_0 = 5.9\,\mathrm{m\,s}^{-1}$.

3.3. Dissipation rate estimates

According to the main Kolmogorov hypothesis, at sufficiently high wave numbers the statistical structure of turbulence has a universal form; the scaling parameters depend only upon ε, the dissipation rate of TKE, and upon ν, the kinematic viscosity. This hypothesis implies that at high wave numbers the turbulence is locally isotropic. The one-dimensional velocity spectrum in the "inertia-viscous subrange" that was taken by a sensor moving in the x direction is as follows (Stewart and Grant, 1962):

$$E_u(k_x) = (\varepsilon\nu^{-5})^{1/4} F_{\mathrm{K}}(k_x\eta), \tag{2}$$

where E_u is the longitudinal (in the x direction) velocity spectrum, k_x is the wave number in the x direction ($k_x = 2\pi f/U_0$ by Taylor's hypothesis), F is a universal function of its non-dimensional argument $k_x\eta$, and $\eta = \nu^{3/4}\varepsilon^{-1/4}$ is the Kolmogorov internal scale of turbulence. In the inertia interval ($k_x\eta \ll 1$), (2) reduces to $E_u(k_x) = \alpha_1\varepsilon,^{2/3}k_x^{-5/3}$ where dimensionless constant $\alpha_1 = 0.5$.

Several interpolation formulas of the universal function F_{K} can be found in the literature on turbulence (Novikov, 1961; Hinze, 1975; Oakey, 1982; Moum et al., 1995). In this paper, we will use the form of function F_{K} as empirically determined by Nasmyth (1970; cf. Oakey, 1982), which has been used in many studies on oceanic turbulence.

The theoretical spectrum of turbulence and its fit to a measured velocity spectrum using the

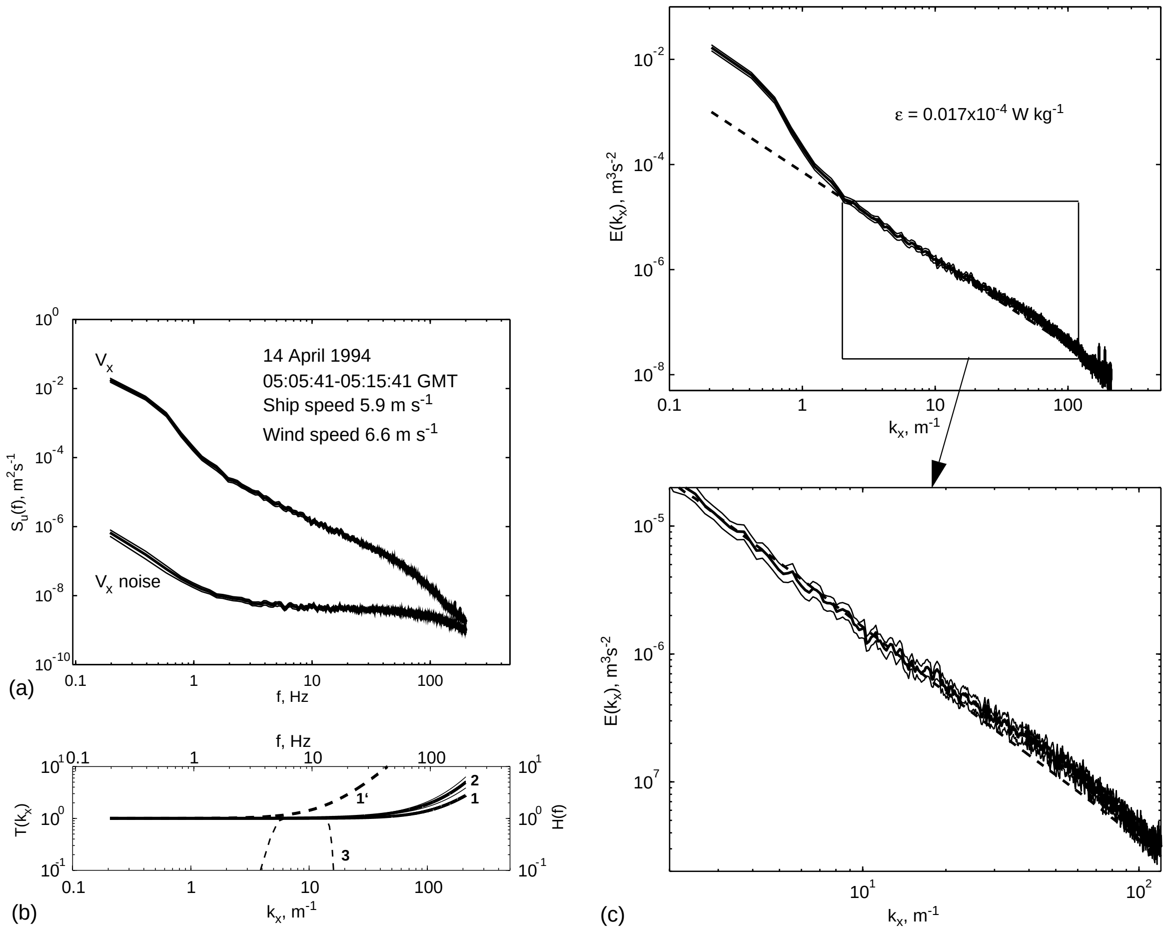

Fig. 6. (a) Spectrum of the velocity signal V_x after processing with the Wiener filter in comparison with the spectrum of electronic noise measured in the laboratory tank. Thin lines represent 95% confidence intervals. (b) Line 1 is the correction for anti-alias filter for 400-Hz sampling rate; line 1′ is the correction for 40-Hz sampling rate; curve 2 is the correction for the spatial averaging of the sensor (thin lines indicate the error interval in determining the sensor's transfer function in laboratory); curve 3 (dashes) shows the frequency range that will be used for calculation of dissipation rate from short velocity segments. (c) Theoretical spectrum of turbulence and its fit to the experimental spectrum using the Stewart and Grant (1962) techniques. Dashed line is the Nasmyth turbulence spectrum, bold line is the experimental velocity spectrum, and thin lines indicate 95% confidence limits. The segment marked by a rectangle is shown in more detail.

Stewart and Grant (1962) techniques are shown in Fig. 6c. The measured spectrum was taken as a frequency spectrum (Fig. 6a); then, it was converted into the wave-number spectrum according to Taylor's hypothesis and transfer functions for anti-alias filter and spatial averaging (Fig. 6b). The theoretical spectrum in Fig. 6c corresponds to $\varepsilon = 1.7 \times 10^{-6}\,\mathrm{W\,kg^{-1}}$.

The large deviation from the theoretical turbulence spectrum at the left (Fig. 6c) is due to the surface-wave and ship-pitching disturbances, which is consistent with the results of Stewart and Grant (1962). There is also a slight difference between the experimental and theoretical spectra in the wave-number range from 20 to $120\,\mathrm{m}^{-1}$. This is presumably an effect of the rapid flow distortion produced by the pressure wave in front of the moving ship. Recently, Fornwalt et al. (2002) modeled this effect numerically and found that the rapid flow distortion results in the net production of TKE concentrated at relatively small scales, which affects the velocity spectrum principally at high wave numbers. Note that the observed deviation might also be introduced by the correction factor for the probe spatial resolution that is known with a 20% accuracy (Fig. 6b). Similar to the disturbance from surface waves, this deviation should not affect the dissipation rate estimate made with the Stewart and Grant (1962) technique.

The uncertainty of the ε estimation due to spectral scatter is small in this example because confidence intervals are small. The spectral scatter, however, is not the only source of error at the dissipation rate estimation. The other errors are introduced by the uncertainty of the instrument towing speed and probe calibration. As we analyze only the data that satisfy Taylor's hypothesis of frozen turbulence, the fluctuation of the towing speed does not exceed 10%. The calibration coefficient for the velocity probe is known with a 5% accuracy. Not included are the errors associated with the assumption of isotropy that are implicit in (2), which alone may introduce a 50% error (Oakey and Elliott, 1982). The individual estimates of ε are therefore considered to be known within a factor of 2.

The dissipation rates calculated from records that are longer than the ship's pitching period are in fact averages over the probe depth range. In the near-surface layer of the ocean (where the vertical profile of dissipation rate can be a non-linear function of depth) this may result in additional errors in the calculation of ε. To address this problem, an alternative technique has been developed: dissipation rates are estimated from short segments, which allows them to be sorted on depth.

3.4. Calculation of dissipation rate from short segments

Calculation of the dissipation rate from short segments consists of the following steps:

(a) Each 10-min V_x record is edited with the processing algorithm described in Soloviev et al. (1995) to remove the segments when the probes surface or enter bubble clouds. Continuous segments of $\Delta t_c \geqslant 5$ s are identified and processed with a 60-weight Wiener filter (to remove the vibration contamination) and band-passed with a Finite Impulse Response (FIR) filter. The transfer function of the band-pass filter is shown in Fig. 6b. The 4–16 Hz frequency band is selected to minimize the influence of surface waves and ship's pitching from one side and possible rapid flow distortion and the uncertainty in the probe's spatial resolution from the other side.

(b) The variance, $\vartheta_u = \sum_1^{N_s}(V'_x - \langle V'_x \rangle)^2/N_s$, is calculated by averaging over $\Delta t_b = 0.1$ s long, 50% overlapping segments, where V'_x is the fluctuation velocity signal processed with the band-pass (4–16 Hz) filter, $N_s = f_s \Delta t_b$, and f_s is the sampling rate (either 400 or 40 Hz), and $\langle\ \rangle$ denotes an average over segment Δt_c. Note that $\langle V'_x \rangle \approx 0$ because $f_l \Delta t_c \gg 1$, where f_l is the lower cut-off frequency of the band-pass filter ($f_l = 4$ Hz).

(c) The theoretical variance ϑ_t is defined as a function of the dissipation rate ε as follows:

$$\vartheta_t(\varepsilon) = \int_0^\infty H_{hp}(f) H_{lp}(f) S(f;\varepsilon)\, df, \tag{3}$$

where $H_{bp}(f)$ is the transfer function of the band-pass FIR filter, $H_{lp}(f)$ is the transfer function of the anti-aliasing filter, $S(f;\varepsilon) = 2\pi U_0^{-1} E(k_x;\varepsilon)'$, $E''(k_x;\varepsilon)' = T(k_x)E(k_x;\varepsilon)$, $T(k_x)$ is the transfer function characterizing the probe's spatial averaging, $E(k_x;\varepsilon)$ is calculated from (2) and the Nasmyth spectrum, and wave number $k_x = 2\pi f U_0^{-1}$. The transfer functions, $H_{bp}(f)$, $H_{lp}(f)$, and $T(k_x)$, are described in the previous section (Section 3.3) and shown in Fig. 6b.

(d) In order to estimate ε, the equation

$$\vartheta_u = \vartheta_t(\varepsilon), \tag{4}$$

is solved by an iteration method, where $\vartheta_t(\varepsilon)$ is determined with the discrete version of integral (3). The iteration process starts from an initial dissipation rate $\varepsilon = 1.2 \times 10^{-12}$ W kg^{-1} and finishes at the value of ε that satisfies (4) with a 1% accuracy.

(e) The dissipation rate estimates obtained from 0.1-s segments are then ensemble averaged within overlapping 10-cm depth bins over the 10-min record segments. In order to account for the intermittent nature of turbulence, the mean dissipation rate and the confidence intervals are calculated from formulas (C.2) and (C.3) given in Appendix C. These formulas assume a lognormal distribution of the turbulence dissipation rate.

Note that the fluctuation of the mean flow speed $r = \mathrm{std}(U/U_0)$ for a 0.1 s period is substantially smaller than for a segment enclosing the full pitching period. During the EQ-3 cruise, r was 3% on average and never exceeded 7%. This reduction of r facilitated the use of Taylor's hypothesis of frozen field under conditions of high seas and strong pitching of the ship.

Fig. 7a and b demonstrates two examples of the averaged vertical profile of dissipation rate ε obtained with this algorithm. The threshold for the minimum number of points for averaging was set at $N_{\min} = 25$. The example shown in Fig. 7b was taken under high wind and wave conditions ($U_{15} = 19\,\mathrm{m\,s^{-1}}$, $H_s = 3.3\,\mathrm{m}$). The confidence intervals in Fig. 7b are bigger than in Fig. 7a in part because of the larger percentage of points removed from averaging of the probe surfacing or entering bubble clouds.

For further analysis, we will use the dissipation rates calculated according to the method described in this section. This method is similar to that of Yamazaki and Lueck (1990) and Prandke and Stips (1996) and is an alternative to the integration method of Wesson and Gregg (1994) and Moum et al. (1995). The shortest averaging scale that produced reasonable dissipation estimates in Yamazaki and Lueck (1990) was only three Kolmogorov length scales (i.e., less than 1 cm). The initial averaging length scale in our method is $\Delta L = U_0 \Delta t_b \sim 50\,\mathrm{cm}$, which exceeds the three Kolmogorov scales (here $U_0 \sim 5\,\mathrm{m\,s^{-1}}$ is the ship speed, and $\Delta t_b = 0.1\,\mathrm{s}$ is the averaging time scale).

The dissipation rates calculated for the month-long COARE EQ-3 cruise are plotted in Fig. 8 as a function of wind speed. The cases when the ship speed was less than $2\,\mathrm{m\,s^{-1}}$ or the ship course or speed varied more than 10% are excluded from these statistics. Note that the data in Fig. 8 are not yet sorted on depth.

The equivalent electronics noise level of the velocity sensor $\varepsilon_n = 1.8 \times 10^{-10}\,\mathrm{W\,kg^{-1}}$ shown in Fig. 8 by a horizontal line was obtained by processing the laboratory noise record via steps (a) through (d). According to Fig. 8, this noise level is much less than the dissipation rate that is typically observed in the near-surface layer of the ocean. No correction for the electronics noise is therefore required.

Ship's pitching and surface waves induce fluctuations of angle α between the flow direction and the probe's longitudinal axis. At large angles ($\alpha > 45°$), the 40 mm diameter tip of the EM probe containing sensing electrodes may start shedding vortices, which are the source of additional, hydrodynamic noise. In the example shown in Fig. 6a, the ship speed $U_0 = 5.9\,\mathrm{m\,s^{-1}}$; disturbance with a 40-mm wavelength translates into a frequency $f = 150\,\mathrm{Hz}$. There are several, relatively small but persistent spectral peaks observed on the velocity spectrum at $f > 140\,\mathrm{Hz}$ (Fig. 6a). These peaks are not observed on the noise spectrum taken in the laboratory (motionless water) and are supposedly due to the hydrodynamic noise of the sensor. (Remember that we use here the frequency range from 4 to 16 Hz for dissipation rate estimates.)

When the winds are almost zero, one would expect the turbulence level to be quite low and the dissipation rate estimates could be close to the noise level of the sensor in situ (electronic plus hydrodynamic noise). Under low wind-speed conditions yet strong shear currents associated with stratification often develop in the near-surface layer of the warm pool area. This results in non-zero dissipation rates even under low wind-speed conditions (Soloviev et al., 2001). In addition, nighttime convection due to surface cooling can maintain the turbulence energy dissipation rate at some non-zero level, depending on the ocean surface cooling rate (Lombardo and Gregg, 1989). (See a dissipation rate estimate due to convection $\varepsilon_c \approx 1.6 \times 10^{-7}\,\mathrm{W\,kg^{-1}}$ in Fig. 8.)

Fig. 8 shows the mean dissipation rate converging between 2×10^{-7} and $2 \times 10^{-6}\,\mathrm{W\,kg^{-1}}$

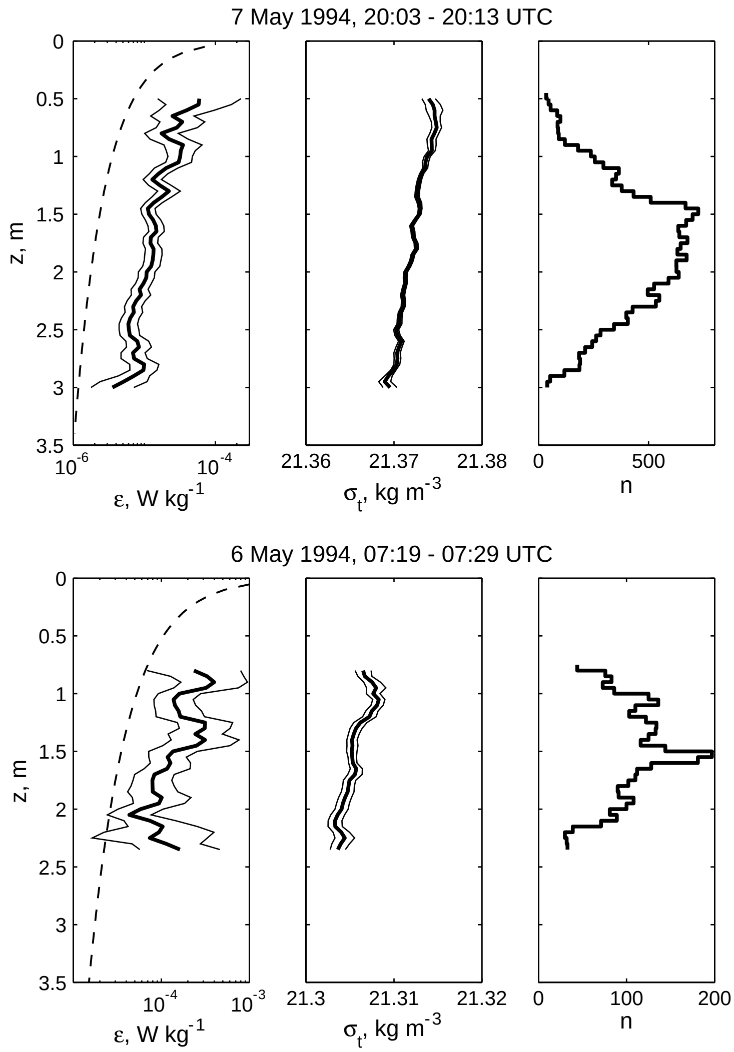

Fig. 7. Vertical profiles of dissipation rate ε and σ_t averaged within 5-cm depth bins over a 10-min bow record segment. Thin lines are 95% confidence intervals calculated from (C.3). Dashed line is the logarithmic layer prediction. Number of points n in each depth bin is also shown. (a) Wind speed $U_{15} = 9.4\,\mathrm{m\,s^{-1}}$, significant wave height $H_s = 1.8\,\mathrm{m}$; (b) $U_{15} = 19\,\mathrm{m\,s^{-1}}$ and $H_s = 3.3\,\mathrm{m}$.

toward the low wind-speed condition, and a relatively small number of points are below $1\times10^{-7}\,\mathrm{W\,kg^{-1}}$. The minimum dissipation rate, $\varepsilon_{min} = 1\times10^{-8}\,\mathrm{W\,Kg^{-1}}$, in Fig. 8 could be interpreted as an upper estimate of the sensor noise level in situ. Note that ε_{min} is still much smaller than the turbulence levels observed in the near-surface layer of the ocean under moderate and high wind-speed conditions (Fig. 8).

For comparison, Moum and Caldwell (1994) observed the mean dissipation in the warm pool area converging between 5×10^{-8} and $1\times10^{-6}\,\mathrm{W\,Kg^{-1}}$ under low wind-speed conditions (though, at a somewhat larger depth of 6 m). The minimum dissipation rate at the 6 m depth observed by Moum and Caldwell (1994) was $2\times10^{-8}\,\mathrm{W\,Kg^{-1}}$.

To elucidate the possible influence of surface waves on the dissipation rate estimation, we

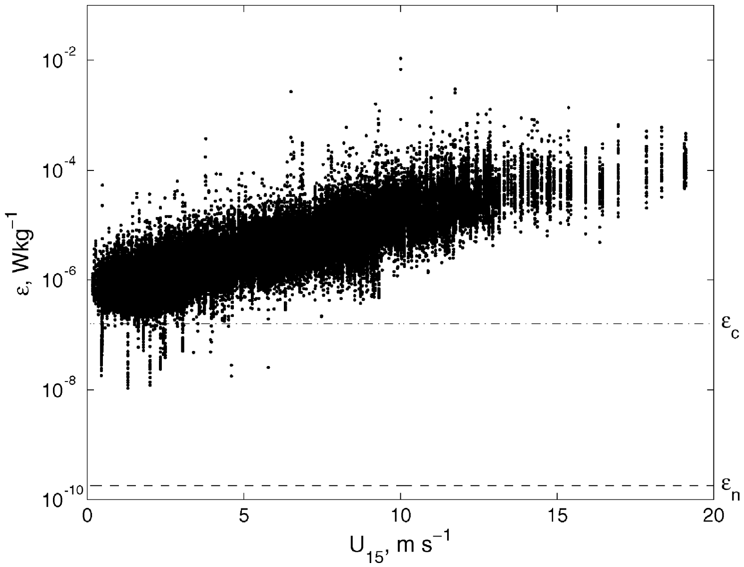

Fig. 8. Month-long data set of ε observed with the bow sensors during COARE EQ-3 versus wind speed U_{15} at a 15-m height. Each point represents a 10-min average (no sorting on depth yet on this graph). The electronic noise of the sensor is indicated as a horizontal dashed line $\varepsilon_n = 1.8 \times 10^{-10}\,\mathrm{W\,kg^{-1}}$. The dissipation rate of TKE due to gravitational convection, ε_c, calculated according to formula (12) for constant $Q_0 = 200\mathrm{W\,m^{-2}}$ is shown as a horizontal point-dashed line.

calculated the wave kinetic energy in the wave-number band that is used for dissipation rate estimates here. The theoretical variance was calculated from the Pierson and Moskowitz (1964) spectrum (multiplied by ω^2, where $\omega = 2\pi f$), surface-wave dispersion relationship $k = \omega^2/g$, the transfer function of the band-pass filter (shown in Fig. 6b, curve 3), and the depth attenuation factor, $\exp(-2kz)$. The theoretical variance was then processed via steps (a) through (d) to obtain an error estimate, ε_w. The relative error, $\varepsilon_w/\varepsilon$ exceeded a 10% level only in 0.2% of all cases collected during the EQ-3 cruise. These points were removed from the analysis; this, however, does not affect in any significant way the average dissipation rate profile.

4. Wave-enhanced turbulence

Small-scale turbulence in the upper layer of the open ocean is generated by convection, shear, and surface-wave breaking. The upper ocean turbulence may be substantially affected by the diurnal cycle and precipitation effects (Gregg et al., 1984; Smyth et al., 1996; Wijesekera and Gregg, 1996; Wijesekera et al., 1999; Soloviev et al., 2001) and by spatially coherent organized motions like Langmuir cells, billows, ramp-like structures, etc. (Thorpe, 1985; Soloviev, 1990; Plueddemann et al., 1996; Li and Garrett, 1997).

In addition to wave breaking, the shear that develops at the bottom of a shallow diurnal or rain-formed mixed layer can greatly increase the turbulence generation (though on relatively small scales) and thus the turbulence dissipation. Based on the measurements made during TOGA COARE by Moum and Caldwell (1994), Soloviev et al. (2001) found a maximum dimensionless dissipation rate of TKE near the bottom of the mixing layer $\varepsilon\kappa z/u_*^3 \sim 500$, which substantially exceeds the log layer prediction, $\varepsilon\kappa z/u_*^3 = 1$. (Here ε is the dissipation rate, κ is Von Karman's constant, and z is the depth. The mixing layer depth in Soloviev et al. (2001) is defined from criteria $Ri = Ri_{cr} = 0.25$, where Ri is the gradient Richardson number. Note that the strong increase of dimensionless dissipation rate near the bottom of the mixed layer is not inconsistent with the decrease of dimensionless mixing coefficient $K_m/(\kappa z u_*)$ because K_m also depends on the turbulent mixing length scale, which rapidly decreases at $Ri \to Ri_{cr} \sim 0.25$. In view of this result, the anomalously high dissipation rate, $\varepsilon \sim 10^3 u_*^3/(\kappa z)$, observed by Kitaigorodskii et al. (1983) in the near-surface layer of Lake Ontario at a $5.4\,\mathrm{m\,s^{-1}}$ wind speed could be explained by stratification effects rather than by the turbulence enhancement due to surface waves, as it was initially interpreted.

During the EQ-3 cruise, we could not measure the gradient Richardson number in the near-surface layer of the ocean (it is still a challenge) and therefore might not identify precisely the cases when stratification effects were important. In this paper, we will analyze only the data obtained under high wind-speed conditions, when the upper few meters of the ocean are usually well mixed by breaking waves (the wave-breaking threshold is typically 6–$7\,\mathrm{m\,s^{-1}}$). In a few cases with strong rainfalls and squalls observed during the EQ-3 cruise, the salinity stratification in the near-surface layer of the ocean was not negligible even under high wind-speed conditions. We removed these cases from the analysis using the criterion $N^2 > 5 \times 10^{-6}\mathrm{s}^{-2}$, where N is the Brunt–Vaisala frequency.

Below we analyze the EQ-3 turbulence data using the Craig and Banner (1994) and Terray et al. (1996) models. The Craig and Banner (1994) model explicitly includes both the wave-breaking and shear-generated turbulence terms. The Terray et al. (1996) model describes only wave-breaking turbulence; the shear-generated turbulence is treated separately.

The following dimensionless expression can be derived from formula (B.5) in Appendix B representing an analytical approximation of the Craig and Banner (1994) model:

$$\varepsilon' \approx 1 + 94.8\, z'^{-2.4}, \tag{5}$$

where $\varepsilon' = \varepsilon\kappa(z+z_0)/u_*^3$, ε is the dissipation rate, κ is the Von Karman's constant ($\kappa = 0.4$); $z' = (z + z_0)/z_0$, z is the depth (distance to the ocean surface), z_0 is the surface roughness length scale from the water side. In these coordinates, dissipation rates in agreement with wall layer theory fall on the line $\varepsilon' = 1$.

The surface roughness from the water side z_0 is a critical but still poorly known parameter in modeling the near-surface turbulence. It depends both on the physics of the turbulent boundary layer and on the properties of the sea surface. Bye (1988) proposed to use the Charnock (1955) type relationship for z_0,

$$z_0 = a u_*^2/g. \tag{6}$$

According to the near-surface velocity profiles measured by Churchill and Csanady (1983) and Csanady (1984), $a = 1400$. These observations were taken under light winds (wind speeds at 3 m less than $5\,\mathrm{m\,s^{-1}}$). Terray et al. (1996) concluded that a is much larger ($\sim$150,000). A higher magnitude of a also follows from the modeling study of the near-surface circulation in Knight Inlet by Stacey (1999) who noted that a may depend on wave age. Alternatively, Terray et al. (1996) proposed z_0 to be parameterized via the significant wave height, H_s:

$$z_0 = cH_s, \tag{7}$$

where $c \sim 1$. (As we will see later, the data from TOGA COARE suggest that $c \approx 0.6$.) Gemmrich and Farmer (1999a) found that during their experiment the near-surface temperature profile was well approximated at a constant value $z_0 = \mathrm{const} \approx 0.2\,\mathrm{m}$.

In Fig. 9a, the COARE EQ-3 turbulence dissipation rates and the Craig and Banner (1994) model are plotted together in dimensionless coordinates $\varepsilon' = \varepsilon\kappa(z+z_0)/u_*^3$ and $z' = (z+z_0)/z_0$, where z_0 is parameterized with formula (6). The wall layer prediction is shown by the dashed vertical line, $\varepsilon' = 1$. The average dissipation profile in Fig. 9b (bold line) is calculated according to formula (C.2). The confidence intervals are calculated from formula (C.3) and are shown with thin lines. The fit between the field and model data demonstrated in Fig. 9b is obtained at $a = 90{,}000$. Further tuning of constant a does not improve the agreement between the experimental data and theory.

In Fig. 10, the same experimental data and the same model are shown for the surface roughness

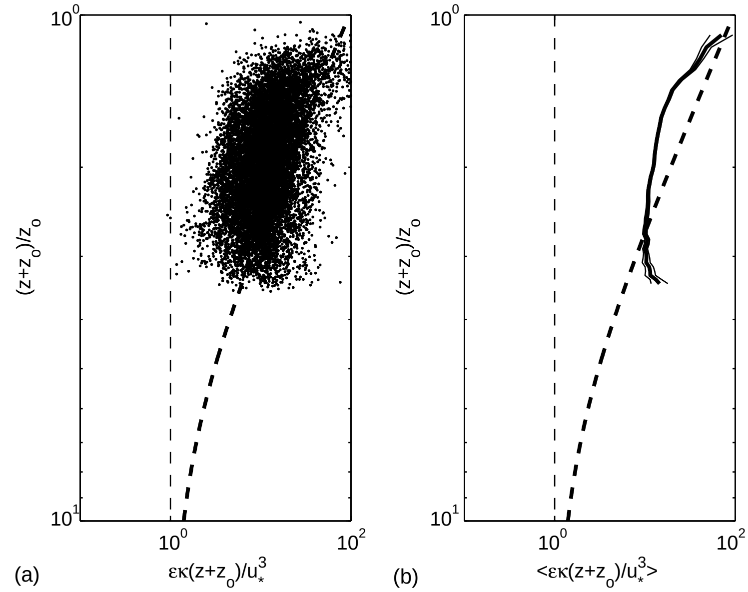

Fig. 9. Dimensionless dissipation rate of TKE, $\tilde{\varepsilon} = \varepsilon\kappa(z + z_0)u_*^{-3}$, versus dimensionless depth, $\tilde{z} = (z + z_0)/z_0$ at $U_{15} > 7\,\mathrm{m\,s^{-1}}$: (a) 10-min averages (points), (b) average profile over COARE EQ-3 cruise (thin lines represent the 95% confidence interval). The vertical dashed line is the logarithmic layer model; the bold dashed curve is the approximation formula (5) for the Craig and Banner (1994) model with the surface roughness length from water side parameterized as $z_0 = au_*^2/g$, where $a = 90{,}000$.

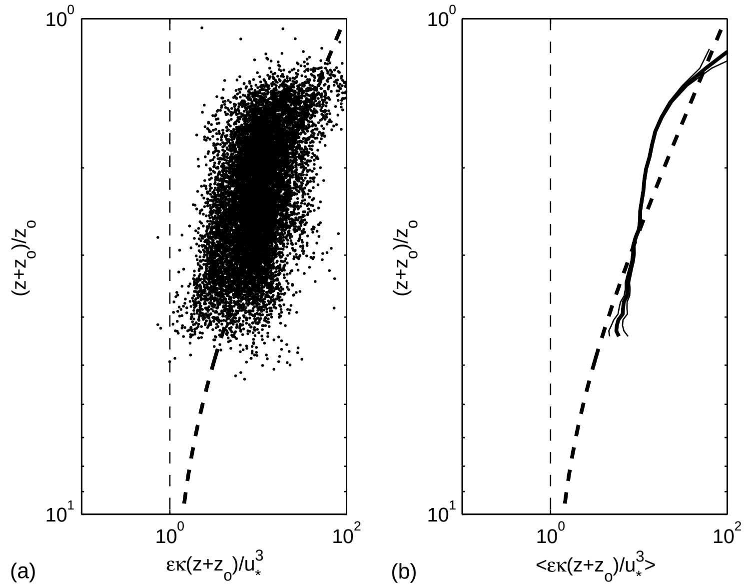

Fig. 10. Same as in Fig. 9 but with the surface roughness length from water side parameterized as $z_0 = cH_s$ where $c = 0.6$.

length from water side parameterized according to Eq. (7) of Terray et al. (1996) $z_0 = cH_s$, where H_s is the significant wave height and $c = 0.6$. In this case, the agreement between the data and model is better than in Fig. 9. Very close to the ocean surface a substantial part of the data was removed from the analysis because of the bubble disturbance to the measurements. The editing procedure thus might bias average dissipation rate estimates close to the ocean surface because bubble areas are associated with the most energetic events (wave breaking). To determine the constant c, we therefore used the deeper part of the experimental profile. This constant would be smaller if we used a near-surface part of the profile.

According to Pierson and Moskowitz (1964), for the saturated surface-wave spectrum, $H_s = 4\sigma_\eta = 1.576 \times 10^5 u_*^2/g$. Assuming that for saturated wave conditions parameterizations (6) and (7) should converge (i.e., $z_0 = cH_s = au_*^2/g$) one can find that $c = 0.6$ corresponds to $a = 94,560$. This is consistent with $a = 90,000$ obtained from the fit of the Craig and Banner (1994) model to the field data shown in Fig. 9.

From comparison of Figs. 9 and 10 it follows that the Terray et al. (1996) parameterization of surface roughness via significant wave height (7) provides a better fit to the Craig and Banner (1994) model to the field data than the Charnock (1955) type parameterization (6).

We have also compared our data with the Craig and Banner (1994) model using a constant value of the surface roughness length scale from the water side. In this case, the fit to the experimental data does not show improvement compared to the Terray et al. (1996) parameterization (7).

The Craig and Banner (1994) model uses the boundary condition for the turbulent flux of the kinetic energy in the form

$$F = \alpha u_*^3, \tag{8}$$

where α is assumed in model calculations to take a constant value of 100. This parameterization was found to be relatively insensitive to the sea state for wave ages embracing wind seas from inverse age $u_{*a}/c_p < 0.075$ to fully developed situations (Terray et al., 1996). At $u_{*a}/c_p < 0.075$, α is no longer constant and depends on the wave age.

Terray et al. (1996) hypothesized that under high wind-speed conditions, the dependence of the dissipation rate on wave age is manifested entirely through its dependence on the scaling variables H_s and F. Based on dimensional analysis and tower-based data collected in Lake Ontario, Terray et al. (1996) proposed the following parameterization for the dissipation rate ε:

$$\varepsilon H_s/F = \begin{cases} 0.3(z/H_s)^{-2} & \text{at } z < 0.6H_s, \\ 0.83 & \text{at } z \geqslant 0.6H_s, \end{cases} \tag{9}$$

where H_s is the significant wave height, F is the flux of the TKE at the air–sea interface, and z is the depth.

The Craig and Banner (1994) model (5), with the surface roughness length from water side parameterized according to Eq. (7) of Terray's et al. (1996) $z_0 = cH_s$ and with the turbulence flux of the kinetic energy according to (8), can be rescaled as follows:

$$\varepsilon H_s/F = \kappa^{-1}\alpha^{-1}(c + z/H_s)^{-1} \times [1 + 4.56(1 + c^{-1}z/H_s)^{-0.8}]^3. \tag{10}$$

Model (9) describes only the wave-breaking component; the shear-generated turbulence should be treated separately. Model (10) includes both shear-generated and wave-breaking turbulence.

Fig. 11a documents the EQ-3 data for high wind-speed conditions scaled according to Terray et al. (1996). Models (9) and (10) and the logarithmic layer model are also shown. The horizontal point-dashed line in Fig. 11a represents the depth of the layer, $H_{50} = 0.6H_s$, within which 50% of the wave energy dissipates according to the Terray et al. (1996) model (9). In the Craig and Banner (1994) model (10), 50% of the wave induced turbulence energy dissipates within the layer, $h_{50} \approx z_0/3$ (see Appendix B). For z_0 parameterized with (7) this corresponds to the depth, $h_{50} \approx cH_s/3 \approx 0.2\,H_s$, which is 3 times smaller than H_{50}.

According to Fig. 11a, the near-surface dissipation rates are in a better agreement with the Craig and Banner model (10) using Terray's et al. (1996) parameterization (7) than with the original Terray et al. (1996) model (9). Note that no tuning coefficients are available in the original Terray et al. (1996) model. Model (10) (fitted to the EQ-3 data as shown in Fig. 11a) predicts lower than model (9) dissipation rates in the layer, $z > 0.4H_s$; above this layer, model (10) demonstrates larger dissipation rates than (9).

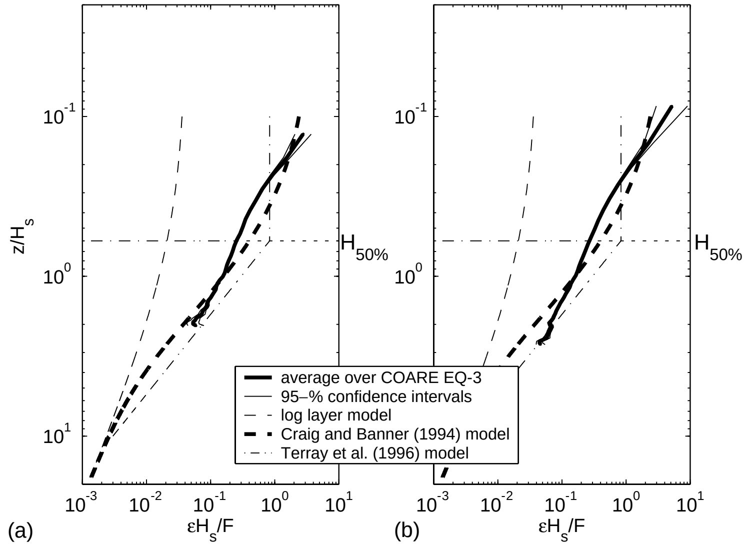

Fig. 11. Normalized dissipation rate, $\varepsilon H_s/F$, versus dimensionless depth, z/H_s. (a) wind-speed range from 9.5 to 19.1 m s^{-1}; (b) same but for wind-speed range from 7 to 19.1 m s^{-1}. The Craig and Banner (1994) dependence is calculated with surface roughness from water side parameterized as $z_0 = 0.6\,H_s$.

A possible reason for this difference (as suggested by one of the anonymous reviewers of this paper) is the use of the wave-following versus fixed coordinate system. If the wave-breaking energy substantially dissipates above the trough line, and the vertical dissipation rate profile is a non-linear function of depth, then the difference between fixed and wave-following measurements is significant. For instance, in a fixed coordinate system it is practically impossible to study near-surface layers with a thickness less than the surface-wave height. In fact, any observational point between the wave trough and crest will alternate between water and air. Therefore, in order to study turbulence above the trough line, a wave-following coordinate system should be used. In this paper, we follow Csanady's (1984) suggestion to analyze the near-surface data in the coordinate system connected to the ocean surface. The Craig and Banner (1994) model is consistent with the Csanady (1984) concept. The Terray et al. (1996) model, which is originally fitted to the tower-based data, would produce a different dissipation profile in the wave-following coordinate system.

Two other possible reasons for unresolved differences between (9) and (10) have been mentioned in Section 3.1. They can be summarized as follows: (1) The standard Taylor hypothesis of frozen field cannot be directly applied for the turbulence analysis of the tower-based measurements because the velocity fluctuation is not small relative to the mean flow; (2) Non-linear components of surface waves, which could not be removed from the tower-based velocity records, might result in an overestimation of ε.

It should be noted that there is no reliable estimate of the average dissipation rate within the wave-stirred layer $z<0.6H_s$ either in Terray et al. (1996) or in our work. Terray et al. (1996) could not make measurements at $z<0.6H_s$ because their sensors had to be positioned below wave troughs, and the data were analyzed in a fixed coordinate system. The constant dissipation $\varepsilon = 0.83F/H_s$ rate that is set in (9) for $z<0.6H_s$ is not based on any experimental data; it results from energy constraints. In our work, the dissipation data were averaged in a wave-following coordinate system and were available starting from a depth $z = 0.1H_s$. The averaged dissipation rate in the layer stirred by breaking surface waves could, however, be biased because of extensive editing of the bubble-disturbed segments. This editing procedure might exclude the most energetic turbulence events associated with breaking waves from the averaging statistics. The experimental dissipation profile systematically deviates from model (10) at $z<0.6H_s$ (Fig. 11a). In the layer $0.1H_s<z<0.6H_s$, the integral energy dissipation rate ($\int \varepsilon(z)\,dz$) is about 5 times less than that predicted by model (10). This suggests that during our measurements about 80% of the wave energy dissipating in the layer stirred by breaking waves might be unaccounted for because of bubble disturbances. Though we are using here the averaging technique that accounts for the turbulence intermittency (see Appendix C), it nevertheless may not completely compensate for editing bubble-disturbed segments, because these disturbances are largely correlated with the dissipation rate peaks. For the same reason, the confidence intervals calculated from (C.3) might be underestimated close to the ocean surface.

Fig. 11b shows the same graphs but for the average dissipation rate profile for moderate and high wind-speed conditions ($U_{15}=7$–$19.2\,\mathrm{m\,s^{-1}}$). The experimental profile in Fig. 11b extends to deeper layers than in Fig. 11a. The interpretation of Fig. 11b is, however, hindered because of larger uncertainty in the significant wave height data than in Fig. 11a. In our experiment this uncertainty rapidly increases with the decrease of the wind speed (see Fig. 13).

According to the experimental results presented here (Fig. 11), in the time averaged description the dissipation of 3–20 times larger than the logarithmic layer prediction is observed in the upper few meters of the ocean under moderate and high wind-speed conditions. We interpret these increased turbulence levels as the effect of surface waves breaking. In terms of the Craig and Banner (1994) model fitted to the EQ-3 data, the energy of wave breaking substantially dissipates within only $\sim$20% of the significant wave height.

The Craig and Banner (1994) model (10) is based on the turbulence closure scheme of Mellor and Yamada (1982). There have been reports that this closure scheme does not work well in flows with negligible shear-production (Umlauf and Burchard, 2003). The flow in wave breakers, however, is not shear free: intense air entrainment leads to the formation of a bore-like structure with significant shear (Longuet-Higgins and Turner, 1974). A model of wave-enhanced turbulence incorporating buoyancy effects due to bubbles (yet to be developed) could provide a better insight into the problem.

5. Discussion

One of the key characteristics of turbulence is its intermittency. This is believed to be the main cause for the random scatter of the dissipation rate estimates from this experiment (Figs. 9a and 10a). Gurvich and Yaglom (1967) presented theoretical considerations based on Kolmogorov's idea of intermittent turbulence leading to the conclusion that the dissipation rate of TKE should have a lognormal distribution. Oakey (1985) observed the lognormal distribution of the dissipation rate statistics in the upper ocean mixed layer. Yamazaki and Lueck (1990) discussed the application of lognormal distribution to the oceanic data in detail.

The probability density function (PDF) of dimensionless dissipation rate $\varepsilon H_s/F$ in three overlapping depth ranges for the EQ-3 cruise is shown in Fig. 12, where F is calculated from (8). The near-surface turbulence dissipation data are close to the theoretical lognormal distribution (C.1). The parameter of lognormal distribution $\sigma_{\ln\varepsilon}$ increases toward the ocean surface. The surface-wave-breaking events are highly intermittent in time and space and lead to widening of the pdf close to the ocean surface.

Analysis of shorter time periods or a wider range of wind-speed conditions than in Fig. 12 could reveal other important features. In particular, lowering the wind-speed threshold to $U_{15}=7\,\mathrm{m\,s^{-1}}$ (i.e., averaging over the wind-speed range from 7 to $19.1\,\mathrm{m\,s^{-1}}$) has allowed us to calculate the pdf of dimensionless dissipation rate $\varepsilon H_s/F$ at $z\sim 2H_s$. This pdf reveals a second peak (similar to that reported by Gemmrich and Farmer, 2002). In our case, however, it is difficult to interpret this result because of increased uncertainty in the significant wave height measurement under lower wind-speed conditions (see Fig. 13).

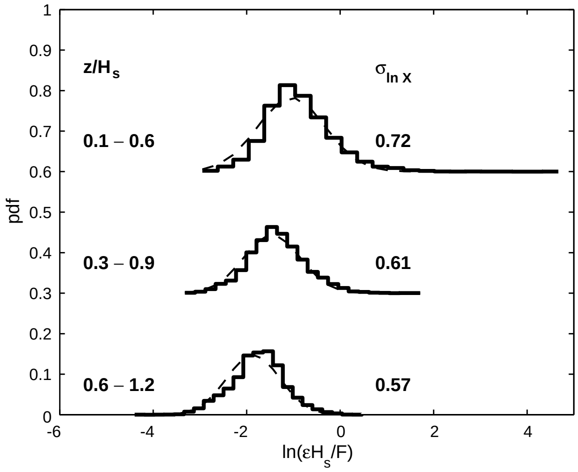

Fig. 12. PDF for the normalized dissipation rate, $\varepsilon H_s/F$, in three overlapping dimensionless depth bins. The surface roughness length from water side, z_0, is parameterized via the significant wave height, H_s (7); the flux of TKE is parameterized with (8). Continuous line is lognormal distribution (C.1). The left column demonstrates the range of z/H_s; the right column shows parameter $\sigma_{\ln x} = \mathrm{std}(\varepsilon H_s/F)$. Zero levels for the pdf in dimensionless depth ranges $z/H_s = 0.1-0.6$ and $0.3-0.9$ are shifted on 0.6 and 0.3, respectively.

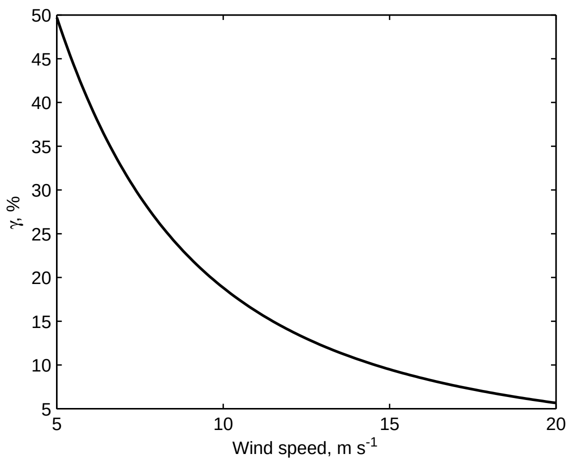

Fig. 13. Relative error γ due to pressure attenuation with depth as a function of wind speed (Eq. A.6) for a sensor at a 1.7-m depth.

Energy budget considerations provide an estimate of the wavelength λ_{diss} where the transition toward the dissipation regime ($\lambda < \lambda_{diss}$) occurs (Kitaigorodskii, 1991):

$$\lambda_{diss} = 2\pi E_0^{2/3}/(Ag), \tag{11}$$

where E_0 is the energy flux from the region of energy input through the non-dissipative region of the wave spectrum toward the dissipation subrange, and $A \approx 1 \times 10^{-4}$ according to the most recent estimates of Gemmrich and Farmer (1999b). Following Gemmrich et al. (1994), we will equate this energy flux to the integral dissipation of wave energy in the upper layer of the ocean due to surface-wave breaking, which in stationary conditions is equal to the flux of the TKE at the air–sea interface, $E_0 = F$. According to Pierson and Moskowitz (1964), for the saturated surface-wave spectrum, the dominating wavelength $\lambda_0 \approx 2\pi B u_*^2/g$, where $B = 8.3 \times 10^5$. From Eqs. (8) and (11), it follows that $\lambda_{diss}/\lambda_0 \approx \alpha^{2/3}/(AB) = 0.26$. This means that breaking waves are much shorter than the dominant wave. Moreover, in the open ocean about 98% of breaking waves are of spilling type, which do not penetrate very deep (Gemmrich and Farmer, 1999b). About 2% of breaking events show deeper penetration. The deeper penetrating events, which are typical for plunging breakers, however, play a minor role in the upper ocean dynamics (even under condition of swell opposing wind waves, when the occurrence of deep penetrating events increases to 10% of the total number of breaking waves). The TKE produced by spilling breakers is localized in a shallow layer (also due to intensive bubble entrainment—see Melville, 1994) and decays fast with depth (Ly and Garwood, 2000; Benilov and Ly, 2002). This is consistent with the COARE EQ-3 results, which suggest that the wave-breaking energy mostly dissipates within ~20% of significant wave height.

In our analysis we have ignored convection as a source of TKE in the near-surface layer of the ocean. According to Lombardo and Gregg (1989), the dissipation rate of TKE due to gravitational convection in the upper ocean

$$\varepsilon_c \sim \alpha g Q_0/(c_p \rho), \tag{12}$$

where α is the thermal expansion coefficient of water, g the acceleration of gravity, Q_0 the net surface heat flux. For $Q_0 = 200\,\mathrm{W\,m^{-2}}$, we obtain $\varepsilon_c \sim 2 \times 10^{-7}\,\mathrm{W\,kg^{-1}}$, which is much less than the typical dissipation rate observed in the upper few meters of the ocean under high wind-speed conditions (Fig. 8). This indicates that in this study the gravitational convection is not a primary source of turbulence.

As suggested by Terray et al. (1996), the flux of the kinetic energy to waves from wind, F, and significant wave height, H_s, are convenient parameters for scaling the dissipation rate of TKE, ε, in the near-surface layer of the ocean. Following Craig and Banner (1994) in our work we have used the parameterization for the flux of the turbulent energy in a simplified form (8), which is valid for developed or nearly developed seas. For young waves, α is no longer a constant and depends on the wave age (Terray et al., 1996; Fig. 6). This is typical for short-fetch wind waves observed in lakes but also is not unusual in the open ocean. Since α is larger for young than for mature waves, the actual flux F might only be larger than that estimated from (8). This would require $c<0.6$ to fit dependence (10) to the data. The contribution of swell waves to the significant wave height, H_s, could have some effect on the non-dimensional dissipation rate, $\varepsilon H_s/F$, and thus on the estimate of c from experimental data.

Although the direct (eddy correlation) measurement of flux F is still a challenge, it can be estimated as the integral of the growth rate over the surface-wave spectrum (Donelan and Pierson, 1987). The Donelan and Pierson (1987) formulation requires information on the frequency-direction spectrum of surface waves, which was not available in our study. Further development of the experimental approach described in this paper therefore requires the measurement of the directional wave spectrum.

Acknowledgements

Anatoli Arjannikov (Granit, St. Petersburg, Russia) provided the technical support for measurements during the *EQ-3* cruise. Mark Baker and Howard Schoeberlein (APL/JHU) tested the turbulence sensors and provided the algorithm for the coherent noise cancellation techniques. Sharon DeCarlo (UH) designed and implemented the data acquisition system, Kevin Kohler (Nova Southeastern University) facilitated data management. Gary Mitchum (USF) and David Stone (UH) provided the TOPEX/POSEIDON data on wind speed and significant wave height for the time period of COARE. Discussion of this project with Eugene Terray, Michael Gregg, Michael Banner, and Alexander Benilov was important for the interpretation of the observations. Eugene Terray kindly provided the updated Matlab code for Craig's and Banner model. The authors thank the anonymous reviewers for their detailed comments. This work was supported by NSF Awards OCE-9525986 and OCE-9730643.

Appendix A. Estimation of significant wave height from bow data

As a surface wave passes over a subsurface position, the displacement of the sea surface η causes a subsurface pressure fluctuation p'. For linear "small-amplitude" surface waves on deep water, the pressure fluctuation decays with depth z according to the formula

$$p' = \rho g \eta \exp(-kz), \tag{A.1}$$

where g is the gravity, ρ the water density, $k = 2\pi/\lambda$ the wave number, and λ the wavelength (Phillips, 1977). According to (A.1), the pressure attenuation with depth is a strong function of the wavelength; short waves are attenuated much faster with depth than longer waves. This implies that for a pressure sensor deployed at a depth z_p, there is a cut-off wavelength λ_m for which waves with $\lambda < \lambda_m$ will be substantially attenuated. The cut-off wavelength can be calculated from the condition

$$k_m z_p \approx 1, \tag{A.2}$$

where $k_m = 2\pi/\lambda_m$.

The bow sensors are mounted at the mean depth $z_p = 1.75$ m; this means that the contribution of waves with $\lambda < 2\pi z_p \approx 10$ m to the significant wave height will be unaccounted for. The associated error can be estimated from the Pierson and Moskowitz (1964) theoretical spectrum $S(\omega)$, which in dimensionless form is as follows:

$$g^3 S(\omega)/U_a^5 = 4.05 \times 10^{-3} (U_a \omega/g)^{-5} \times \exp[-0.74(U_a \omega g)^{-2}], \tag{A.3}$$

where U_a is the wind speed. The variance of the sea-surface displacement that follows from the Pierson and Moskowitz (1964) spectrum is $\sigma_\eta^2 = 2\int_0^\infty S(\omega)\,d\omega = 0.0027U_a^4/g^2$. The variance that is measured by the submerged pressure sensor is estimated as follows:

$$\sigma_m^2 = 2\int_0^\infty S(\omega)\exp(-2kz)\,d\omega, \tag{A.4}$$

where factor $\exp(-2kz)$ describes the depth attenuation, and wave number $k = \omega^2/g$ from linear theory.

The significant wave height (H_s) is defined in the oceanographic literature as the average height of the highest $\frac{1}{3}$ of the waves and is estimated as follows:

$$H_s = 4\sigma_\eta, \tag{A.5}$$

where σ_η^2 is the variance of the sea-surface displacement. The significant wave height measured with a the pressure sensor at a 1.7-m depth is $H_s' = 4\sigma_m$. Relative error due to pressure attenuation with depth is estimated in the following way:

$$\gamma = |H_s - H_s'|/H_s = (1 - \sigma_m/\sigma_\eta). \tag{A.6}$$

For the mean depth of pressure sensor, $z = 1.75$ m, γ as a function of wind speed U_a is shown in Fig. 13.

In order to account for the ship pitching, the vertical component of the acceleration signal can be used. In a coordinate system referenced to the bow sensors, sea-surface displacement $\eta(t)$ due to waves is calculated from the following relationship:

$$\eta(t) = \zeta(t) - \int_0^t \left(\int_0^\tau g_z(t')\,dt' \right) d\tau, \tag{A.7}$$

where ζ is the distance of the sensor to the ocean surface, g_z the vertical component of acceleration measured by the bow sensor, and t the elapsed time.

Since the bow measurements are made from a moving ship, the Doppler effect shifts the dispersion relationship for surface waves and makes it impossible to know about the wave number based on the wave frequency. This limits the use of (A.1). Instead the hydrostatic equation can be used:

$$p - p_a = \rho_w g \zeta, \tag{A.8}$$

where p_a is the atmospheric pressure on the sea-surface level.

Note that the acceleration signal entering Eq. (A.7) is twice integrated; as a result, low-frequency noise of this sensor is strongly emphasized. The acceleration signal $g_z(t)$ is, therefore, high-passed with a 0.05-Hz cut-off frequency. In addition, to reduce the spectral "leakage", the spectrum is initially calculated for the difference, $y(t) = \eta_{tt}(t) = \zeta_{tt}(t) - g_z(t)$, which is then twice integrated in the frequency domain by multiplying the spectrum with a factor of $(2\pi f)^{-4}$.

Fig. 14 shows an example of the pressure fluctuation spectrum $S_p(f)$ (in depth units), spectrum of twice integrated acceleration signal $S_g(f)$, and surface-wave displacement spectrum $S_\eta(f)$ (calculated from the pressure and acceleration bow signals). The variance of the sea-surface displacement σ_η^2 is calculated as a sum of the spectral components $S_\eta(f)$ in the frequency range from 0.04 to 2.5 Hz.

Since the bow measurements are made from the moving ship, the sea-surface displacement spectrum $S_\eta(f)$ is apparently Doppler shifted. The

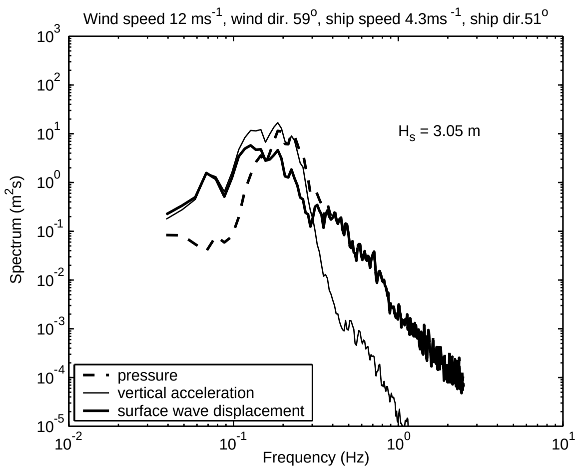

Fig. 14. Pressure (in depth units), double-integrated vertical acceleration, and surface-wave spectra calculated from a 10-min segment of bow signals. The ship was steaming into the wind at 4.3 m s^{-1}. The significant wave height estimated from the surface displacement spectrum is $H_s = 3.05$ m. Since the bow measurements are made from the moving ship, the surface-wave displacement spectrum is apparently Doppler shifted. The significant wave height estimate, H_s, however, is not affected by the Doppler effect.

variance of the sea-surface displacement, however, is invariant to the ship motion in horizontal direction; therefore, the significant wave height estimate, H_s, is not affected by the Doppler shift. The error estimate shown in Fig. 13 is also invariant to the Doppler shift, because the pressure attenuation with depth is determined solely by the wave dynamics and does not depend on measurement techniques. (Note that this is a tentative error estimate because it is derived from the spectrum of fully developed waves.)

Appendix B. Model of wave-enhanced turbulence

Craig and Banner (1994) developed a model that employs the level 2-1/2 turbulence closure scheme of Mellor and Yamada (1982). The surface-wave effects are incorporated into this model via the TKE flux at the air–sea interface, a procedure similar to that of Benilov (1973). Dissipation due to turbulent motion is defined as

$$\varepsilon = q^3/(Bl), \tag{B.1}$$

where q is the velocity scale, l is the length scale, and $B = 16.6$. The length scale is approximated as follows:

$$l = \kappa(z + z_0), \tag{B.2}$$

where $\kappa = 0.4$ is the Von Karman's constant, z is the depth, and z_0 is the surface roughness length from the water side.

For the asymptotic regimes when the shear production (B.3) or diffusion of TKE (B.4) balance dissipation, the dissipation rate is expressed analytically as follows:

$$\varepsilon_{sh} = u_*^3(B/S_M)^{3/4}/(B\kappa(z_0 + z)), \tag{B.3}$$

$$\varepsilon_{wv} = \frac{au_*^3(3B/S_q)^{1/2}(z_0/(z_0 + z))^n}{(B\kappa(z_0 + z))}, \tag{B.4}$$

where $n = (3/k^2BS_q))^{1/2} = 2.4$, $S_M = 0.39$, and $S_q = 0.2$. When both shear production and diffusion are present, the dissipation rate is approximated as a sum of the two asymptotic terms:

$$\varepsilon \approx \varepsilon_{sh} + \varepsilon_{wv} = u_*^3/(B\kappa(z_0 + z))[(B/S_M)^{3/4} + \alpha(3B/S_q)^{1/2}(z_0/(z_0 + z))^n]. \tag{B.5}$$

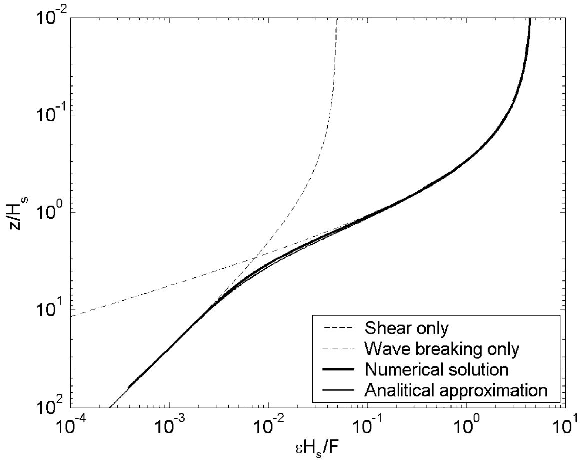

Fig. 15. Steady-state numerical solution of the Craig and Banner (1994) model for a finite-depth layer $H = 100\,\text{m}$, its logarithmic layer (B.3) and wave-breaking (B.4) asymptotes, and an analytical approximation (B.5).

Since adjustment of the turbulence regime to local conditions is a relatively fast process, for the upper few meters of the ocean in many cases it is possible to use a steady-state solution. Fig. 15 demonstrates the numerical steady-state solution of the Craig and Banner (1994) model, asymptotes (B.3) and (B.4), and an analytical approximation (B.5) According to Fig. 15, formula (B.5) approximates the numerical solution very well.

Integration of the vertical dissipation profile given by model (B.4) from $z = 0$ to depth h_{50} (where 50% of the wave energy dissipates) results in the equation for h_{50}, $\int_0^{h_{50}} \varepsilon\, dz = 0.5\alpha u_*^3$ The solution of this equation is $h_{50} = z_0(2^{1/2} - 1) \approx z_0/3$.

The dimensionless constants B and S_M were chosen by Mellor and Yamada (1982) to ensure that at $z_0 = 0$, the logarithmic layer asymptote is achieved. Note that all dimensionless constants (κ, B, S_q, S_M) entering the Craig and Banner model are determined from the fluid mechanics problems that are not related directly to wave-enhanced turbulence.

Appendix C. Lognormal distribution and confidence intervals

The application of lognormal distribution to the analysis of the dissipation rate statistics in the upper ocean is described in detail in Oakey (1985) and Yamazaki and Lueck (1990). Here, we will reiterate the main properties of lognormal distributions. A lognormal distribution of a random variable x is one where $y = \ln x$ is distributed according to a normal law. The PDF of x is

$$f(x) = (x\sigma_{\ln x}\sqrt{2\pi})^{-1} \times \exp[-0.5\sigma_{\ln x}^{-2}(\ln x - \mu)^2], \tag{C.1}$$

where μ and $\sigma_{\ln x}^2$ are the mean and variance of $\ln x$, respectively, and $\sigma_{\ln x}^2$ is called Kolmogorov's intermittency parameter. The expected value of x is then

$$\langle x \rangle = \exp(\mu + \sigma_{\ln x}^2/2). \tag{C.2}$$

The confidence interval for $\langle x \rangle$ is given by

$$\exp(\mu + \sigma_{\ln x}^2/2)\exp(-\eta z_{\alpha/2}) < \langle x \rangle < \exp(\mu + \sigma_{\ln x}^2/2)\exp(\eta z_{\alpha/2}), \tag{C.3}$$

where $\eta = [\sigma_{\ln x}^2/n + 0.5\sigma_{\ln x}^4/(n-1)]^{1/2}$ according to Baker and Gibson (1987); $z_{\alpha/2} = 1.96$ for a 95% confidence interval.

References

Agrawal, Y.C., Terray, E.A., Donelan, M.A., Hwang, P.A., Willimas III, A.J., Drennan, W.M., Kahma, K.K., Kitaigorodskii, S.A., 1992. Enhanced dissipation of kinetic energy beneath surface waves. Nature 359, 219–220.

Arjannikov, A.V., Golubev, Yu.E., Zvickevich, V.A., 1979. Apparatus for velocity measurement in the water flow. USSR Patent N679878. Bulletin of inventions, N30 (in Russian only).

Arsenyev, S.A., Dobroklonsky, S.V., Mamedov, R.M., Shelkovnikov, N.K., 1975. Direct measurements of some characteristics of fine structure from a stationary platform in the open sea. Izvestiya, Fizika Atmosphery i Okeana 11, 845–850 (English translation).

Baker, M.A., Gibson, C.H., 1987. Sampling turbulence in the stratified ocean: statistical consequences of strong intermittency. Journal of Physical Oceanography 17, 1817–1837.

Benilov, A.Yu., 1973. Generation of turbulence in the ocean by surface waves. Izvestiya, Fizika Atmosphery i Okeana 9, 293–303.

Benilov, A.Yu., Filyushkin, B.N., 1970. Application of the linear filtration methods to the fluctuation analysis in the sea upper layer. Izvestiya, Fizika Atmosphery i Okeana 6, 477–482.

Benilov, A.Yu., Ly, L.N., 2002. Modeling of surface waves breaking effects in the ocean upper layer. Mathematical and Computer Modelling 35, 191–213.

Bye, J.A.T., 1988. The coupling of wave drift and wind velocity profiles. Journal of Marine Research 46, 457–472.

Callahan, P.S., Morris, C.S., Hsiao, V., 1994. Comparison of TOPEX/POSEIDON σ_0 an significant wave height distributions to geosat. Journal of Geophysical Research 99, 25015–25024.

Charnock, H., 1955. Wind stress on a water surface. Quarterly Journal of the Royal Meteorological Society 81, 639–640.

Churchill, J.H., Csanady, G.T., 1983. Near-surface measurements of quasi-Lagrangian velocities in open water. Journal of Physical Oceanography 13, 1669–1680.

Csanady, G.T., 1984. The free surface turbulent shear layer. Journal of Physical Oceanography 14, 402–411.

Craig, P.D., Banner, M.L., 1994. Modeling wave-enhanced turbulence in the ocean surface layer. Journal of Physical Oceanography 24, 2546–2559.

Dillon, T.M., Richman, J.G., Hansen, C.G., Pearson, M.D., 1981. Near-surface turbulence measurements in a lake. Nature 290, 390–392.

Donelan, M.A., Pierson, W.J., 1987. Radar scattering and equilibrium ranges in wind-generated waves with application to scatterometry. Journal of Geophysical Research 92, 4971–5029.

Drennan, W.M., Donelan, M.A., Terray, E.A., Katsaros, K.B., 1996. Oceanic turbulence dissipation measurements in SWADE. Journal of Physical Oceanography 26, 808–815.

Emery, W.J., Thompson, R.E., 1998. Data Analysis Methods in Physical Oceanography. Pergamon Press, Oxford, 634pp.

Fairall, C.W., Bradley, E.F., Hare, J.E., Grachev, A.A., Edson, J.B., 2003. Bulk parameterization an air–sea fluxes: Updates and verification for the COARE algorithm. J. Climate 16, 571–591.

Fornwalt, B., Terray, G., Voulgaris, G., Trowbridge, J., 2002. Flow modeling around an autonomous underwater vehicle with applications to turbulence measurements. Ocean Sciences Meeting, 11–15 February 2002, Honolulu, Hawaii (Abstract). EOS, Transactions, American Geophysical Union 83(4, Suppl.), OS143.

Gemmrich, J.R., Farmer, D.M., 1999a. Near-surface turbulence and thermal structure in a wind-driven sea. Journal of Physical Oceanography 29, 480–499.

Gemmrich, J.R., Farmer, D.M., 1999b. Observations of the scale and occurrence of breaking surface waves. Journal of Physical Oceanography 29, 2595–2606.

Gemmrich, J.R., Farmer, D.M., 2002. Near-surface turbulence in the presence of breaking waves. Ocean Sciences Meeting, 11–15 February 2002, Honolulu, Hawaii (Abstract). EOS, Transactions, American Geophysical Union 83(4, Suppl.), OS371.

Gemmrich, J.R., Mudge, T.D., Polonichko, V.D., 1994. On the energy input from wind to surface waves. Journal of Physical Oceanography 24, 2413–2417.

Godfrey, J.S., Houze Jr., R.A., Johnson, R.H., Lukas, R., Redelsperger, J.-L, Sumi, A., Weller, R., 1998. Coupled ocean–atmosphere response experiment (COARE): an interim report. Journal of Geophysical Research 103, 14395–14450.

Greenan, B.J.W., Oakey, N.S., Dobson, F.W., 2001. Estimates of dissipation in the ocean mixed layer using a quasi-horizontal microstructure profiler. Journal of Physical Oceanography 31, 992–1004.

Gregg, M.C., Peters, H., Wesson, J.C., Oakey, N.S., Shay, T.J., 1984. Intense measurement of turbulence and shear in the equatorial undercurrent. Nature 318, 140–144.

Gurvich, A.S., Yaglom, A.M., 1967. Breakdown of eddies and probability distributions for small-scale turbulence. Physics of Fluids 10 (Suppl., Part II), 559–565.

Jones, I.S.F., Kenney, B.C., 1977. The scaling of velocity fluctuations in the surface mixed layer. Journal of Geophysical Research 82, 1392–1396.

Hinze, J., 1975. Turbulence. McGraw-Hill, New York, USA.

Kitaigorodskii, S.A., Donelan, M.A., Lumley, J.L., Terray, E.A., 1983. Wave-turbulence interactions in the upper ocean: Part II. Journal of Physical Oceanography 13, 1988–1999.

Kitaigorodskii, S.A. 1991. The dissipation subrange of wind wave spectra. In: Banner, M.L., Grimshaw, R.H.J. (Eds.), Breaking Waves, UTAM Symposium, Sydney, Australia, 1991, 199–206.

Li, M., Garrett, C., 1997. Mixed layer deepening due to Langmuir circulation. Journal of Physical Oceanography 27, 121–132.

Lombardo, C.P., Gregg, M.C., 1989. Similarity scaling of viscous and thermal dissipation in a convecting surface boundary layer. Journal of Geophysical Research 94, 6273–6284.

Longuet-Higgins, M.S., Turner, J.S., 1974. An entraining plume model of a spilling breaker. Journal of Fluid Mechanics 63, 1–10.

Ly, L.N., Garwood Jr., R.W., 2000. Numerical modeling of wave-enhanced turbulence in the oceanic upper layer. Journal of Oceanography 56, 473–483.

Lukas, R., Webster, P.J., Ji, M., Leetmaa, A., 1995. The large-scale context for the TOGA coupled ocean–atmosphere response experiment. Meteorology and Atmospheric Physics 56, 3–16.

Mellor, G.L., Yamada, T., 1982. Development of a turbulence closure model for geophysical fluid problems. Reviews of Geophysics 20, 851–875.

Melville, W.K., 1994. Energy dissipation by breaking waves. Journal of Physical Oceanography 24, 2041–2049.

Melville, W.K., Matusov, P., 2002. Distribution of breaking waves at the ocean surface. Nature 417, 58–63.

Moum, J.N., Caldwell, D.R., 1994. Experiment explores the dynamics of the ocean mixing. EOS, Transactions, American Geophysical Union 75, 489, 494–495.

Moum, J.N., Gregg, M.C., Lien, R.C., Carr, M.E., 1995. Comparison of turbulence kinetic energy dissipation rates estimates from two ocean microstructure profilers. Journal of Atmospheric and Oceanic Technology 12, 346–366.

Nasmyth, P.W., 1970. Oceanic turbulence. Ph.D. Dissertation, University of British Columbia, Vancouver.

Novikov, E.A., 1961. The energy spectrum of the turbulent flow in an incompressible fluid. Doklady Akademii Nauk SSSR 139 (2), 1961.

Oakey, N.H., 1982. Determination of the rate of dissipation of turbulent energy from simultaneous temperature and velocity shear microstructure measurements. Journal of Physical Oceanography 12, 256–271.

Oakey, N., 1985. Statistics of mixing parameters in the upper ocean during JASIN Phase 2. Journal of Physical Oceanography 15, 1662–1675.

Oakey, N.S., Elliott, J.A., 1982. Dissipation within surface mixed layer. Journal of Physical Oceanography 12, 175–195.

Phillips, O.M., 1977. The Dynamics of the Upper Ocean. Cambridge University Press, Cambridge.

Pierson, W.J., Moskowitz, L., 1964. A proposed spectral form for fully developed wind seas based on the similarity theory of S.A. Kitaigorodsky. Journal of Geophysical Research 69, 5181–5190.

Plueddemann, A.J., Smith, J.A., Farmer, D.M., Weller, R.A., Crawford, W.R., Pinkel, R., Vital, S., Gnanadesikan, A., 1996. Structure and variability of Langmuir circulation during the surface waves processes program. Journal of Geophysical Research 101, 3525–3543.

Prandke, H., Stips, A., 1996. Investigation of microstructure and turbulence in marine and Limnic waters using the MST profiler. European Commission, Joint Research Centre, Space Applications Institute, Technical Note No. I.96.87.

Schoeberlein, H.C., Baker, M.A., 1996. Status report: reduction of motion contamination in TOGA COARE velocity measurements. Technical Report, 13 December 1996, The Johns Hopkins University, Applied Physics Laboratory, Laurel MD 20723, 46pp.

Shinoda, T., DeCarlo, S., Kennan, S., Lukas, R., Santiago-Mandujano, F., Snyder, J., 1995. Shipboard measurements during COARE enhanced monitoring cruises. SOEST Technical Report 95–07, School of Ocean and Earth Science and Technology, University of Hawaii, Honolulu, HI, 205pp.

Smyth, W.D., Hebert, D., Moum, J.N., 1996. Local ocean response to a multiphase westerly wind burst, 1, dynamic response. Journal of Geophysical Research 101, 22495–22512.

Soloviev, A., 1990. Coherent structure at the ocean surface in the convectively unstable conditions. Nature 346, 157–160.

Soloviev, A., Lukas, R., 1996. Observation of spatial variability of diurnal thermocline and rain-formed halocline in the western Pacific warm pool. Journal of Physical Oceanography 26, 2529–2538.

Soloviev, A., Lukas, R., 1997a. Observation of large diurnal warming events in the near-surface layer of the western equatorial Pacific warm pool. Deep-Sea Research I 44, 1055–1076.

Soloviev, A., Lukas, R., 1997b. Sharp frontal interfaces in near-surface layer of the ocean in the western Pacific warm pool. Journal of Physical Oceanography 27, 999–1017.

Soloviev, A.V., Vershinsky, N.V., Bezverchnii, V.A., 1988. Small-scale turbulence measurements in the thin surface layer of the ocean. Deep-Sea Research 35, 1859–1874.

Soloviev, A.V., Lukas, R., DeCarlo, S., Snyder, J., Arjannikov, A., Baker, M., Khlebnikov, D., 1995. Small-scale measurements near the ocean–air interface during TOGA-COARE. Data Report, SOEST-95-05, University of Hawaii, Honolulu, HI, 257pp.

Soloviev, A., Lukas, R., DeCarlo, S., Snyder, J., Arjannikov, A., Turenko, V., Baker, M., Khlebnikov, D., 1998. A near-surface microstructure sensor system used during TOGA-COARE Part I: bow measurements. Journal of Atmospheric and Oceanic Technology 15, 563–578.

Soloviev, A., Lukas, R., Hacker, P., Baker, M., Schoeberlein, H., Arjannikov, A., 1999. A near-surface microstructure sensor system used during TOGA COARE Part II: turbulence measurements. Journal of Atmospheric and Oceanic Technology 16, 1598–1618.

Soloviev, A., Lukas, R., Hacker, P., 2001. An approach to parameterization of the oceanic turbulent boundary layer in the Western Pacific warm pool. Journal of Geophysical Research 106, 4421–4435.

Stacey, M.W., 1999. Simulation of the wind-forced near-surface circulation in knight inlet: a parameterization of the roughness length. Journal of Physical Oceanography 29, 1363–1367.

Stewart, R.W., Grant, H.L., 1962. Determination of the rate of dissipation of turbulent energy near the sea surface in the presence of waves. Journal of Geophysical Research 67, 3177–3180.

Taylor, G.I., 1938. The spectrum of turbulence. Proceeding of the Royal Society of London A 164, 476–490.

Terray, E.A., Donelan, M.A., Agrawal, Y.C., Drennan, W.M., Kahma, K.K., Williams III, A.J., Hwang, P.A., Kitaigorodskii, S.A., 1996. Estimates of kinetic energy dissipation under breaking waves. Journal of Physical Oceanography 26, 792–807.

Thorpe, S.A., 1985. Small-scale processes in the upper ocean boundary layer. Nature 318, 519–522.

Umlauf, L., Burchard, H., 2003. A generic length-scale equation for geophysical turbulence models. Journal of Marine Research, accepted for publication, 2003.

Van Dyke, M., 1982. An Album of Fluid Motion. Parabolic Press, Stanford, CA.

Wesson, J.C., Gregg, M.C., 1994. Mixing in Camarinal Sill in the Strait of Gibraltar. Journal of Geophysical Research 99 (C5), 9847–9878.

Wijesekera, H.W., Gregg, M.C., 1996. Surface layer response to weak winds, westerly bursts, and rain squalls in the western Pacific war, pool. Journal of Geophysical Research 101 (C1), 977–997.

Wijesekera, H.W., Paulson, C.A., Huyer, H., 1999. The effect of rainfall on the surface layer during a westerly burst in the western equatorial Pacific. Journal of Physical Oceanography 29, 612–832.

Yamazaki, H., Lueck, R.G., 1990. Why oceanic dissipation rates are not lognormal. Journal of Physical Oceanography 20, 1907–1918.